On the Vertical Structure of Wind-Driven Sea Currents

VLADIMIR KUDRYAVTSEV

Nansen International Environmental and Remote Sensing Center, St. Petersburg, Russia, and Nansen Environmental and Remote Sensing Center, Bergen, Norway, and Marine Hydrophysical Institute, Sebastopol, Ukraine

VICTOR SHRIRA

Department of Mathematics, Keele University, Keele, United Kingdom

VLADIMIR DULOV AND VLADIMIR MALINOVSKY

Marine Hydrophysical Institute, Sebastopol, Ukraine

(Manuscript received 20 July 2007, in final form 19 February 2008)

ABSTRACT

The vertical structure of wind-driven sea surface currents and the role of wind-wave breaking in its formation are investigated by means of both field experiments and modeling. Analysis of drifter measurements of surface currents in the uppermost 5-m layer at wind speeds from 3 to 15 m s^{-1} is the experimental starting point of this study. The velocity gradients beneath the surface are found to be 2 to 5 times weaker than in the "wall" boundary layer. Surface wind drift (identified via drift of an artificial slick) with respect to 0.5-m depths is about 0.7%, which is even less than the velocity defect over the molecular sublayer in the wall boundary layer at a smooth surface. To interpret the data, a semiempirical model describing the effect of wave breaking on wind-driven surface currents and subsurface turbulence is proposed. The model elaborates on the idea of direct injection of momentum and energy from wave breaking (including micro-scale breaking) into the water body. Momentum and energy transported by breaking waves into the water significantly enhance the turbulent mixing and considerably decrease velocity shears as compared to the wall boundary layer. No "artificial" surface roughness scale is needed in the model. From the experimental fact of the existence of cool temperature skin at the sea surface, it is deduced that there is a molecular sublayer at the water side of the sea surface with a thickness that depends on turbulence intensity just beneath the surface. The model predictions are consistent with the reported and other available experimental data.

1. Introduction

The sensitivity of the ocean–atmosphere system to the processes at the ocean surface and in the few uppermost meters is well known: in particular, the first 2.5 m of water column have the same heat capacity as the entire atmosphere above; more than 40% of the solar radiation is absorbed in the first 10 m (Gill 1982). However, despite persistent efforts of many research groups, the present understanding of links between wind waves, turbulence, and surface shear currents, as well as their role in the momentum and heat exchange processes, is still quite poor (e.g., Thorpe 2004). The relatively slow progress is due to genuine difficulties: comprehensive and precise measurements in sea conditions are still beyond the reach of the existing experimental techniques, while any advance in theoretical modeling requires a new paradigm.

The commonly accepted paradigm is based on the idea of a "wall" turbulent boundary layer beneath the surface, which is affected by the earth's rotation further below; therefore, the shear current is expected to be logarithmic just beneath the surface and then to morph into the Ekman layer specified by an appropriate turbulent viscosity. Field and laboratory measurements systematized and reported by Csanady (1984, see his Fig. 4 and corresponding references) seem to confirm the wall layer analogy (the current velocity profiles are indeed logarithmic). These measurements were taken

Corresponding author address: Vladimir Kudryavtsev, Nansen International Environmental and Remote Sensing Center, 7, 14th line Vasilevskii Ostrov, 199034, St. Petersburg, Russia.
E-mail: vladimir.kudryavtsev@niersc.spb.ru

DOI: 10.1175/2008JPO3883.1

at limited fetches and during gentle-to-moderate wind conditions. Presumably, at these conditions wave breaking did not affect the depth range where the current velocity was measured. On the other hand, the data by Churchill and Csanady (1983) suggest a linear distribution of the mean current velocity just beneath the surface, which was attributed to the wave-breaking effect. The main notable features of these measurements are (i) the effective roughness scale (defined through the mean current profile measurements) greatly (several orders in magnitude) exceeds the value expected for a smooth surface and (ii) velocity defect between the surface and any fixed depth is much less than in the wall turbulent boundary layer.

In contrast to the Csanady (1984) observations, the data from the field measurements carried out by Kitaigorodskii et al. (1983) at Lake Ontario, by Thorpe (1984) at Loch Ness, and by Santala (1991) at the California shelf demonstrate the presence of a pronounced wave-affected nonlogarithmic layer adjacent to the surface, characterized by a low velocity gradient and the penetration depth of about a few times the dominant wave amplitude. Below this layer a logarithmic velocity profile is restored.

Much of the evidence on a wave-affected boundary layer is indirect and is based on measurements of the turbulent kinetic energy dissipation. The wall analogy was found to be definitely inadequate in the presence of breaking waves: the intensity of turbulence measured in extensive field experiments proved to be much higher (Kitaigorodskii et al. 1983; Agrawal et al. 1992; Drennan et al. 1992, 1996; Terray et al. 1996; Soloviev and Lukas 2003; Gemmrich and Farmer 2004). The dissipation rate in the wave-affected layer exceeds 10 to 100 times the values expected from the wall analogy, and the penetration depth of the layer with enhanced turbulence is on the order of the significant wave height. The discrepancy was attributed to the production of turbulence by wind wave breaking, although the specific mechanism of the turbulence enhancement has not been identified.

Closely related and still poorly understood is the problem of sea surface roughness scale (as seen from below). The only consensus is that the roughness scale dramatically (four to six orders of magnitude) exceeds the values expected from either a smooth or a rough wall boundary layer analogy (see, e.g., discussion in Kitaigorodskii 1994 and Craig and Banner 1994). At present, the roughness scale is rather a fitting parameter compared to a real physical quantity subject to a special investigation. As mentioned by many authors, the roughness scale is presumably related to the significant wave height (H_s). Craig and Banner (1994), Stacey (1999), and Soloviev and Lukas (2003) used the roughness scale z_0, proportional to H_s (z_0 is in the range 0.1–8 m) to obtain an agreement between their model simulations and observations; Craig (1996) found that z_0 on the order of centimeters fits both the model predictions and the profiles measured by Cheung and Street (1988) in laboratory conditions. However, such an approach to parameterize z_0 contradicts the existence of a well-known phenomenon—the "cool skin" of the ocean, which is routinely observed at any wind conditions, at least up to the wind speeds when surface foam becomes a dominant surface feature (see, e.g., Sounders 1978; Schlussel et al. 1990). The physical origin of the ocean's cool skin is molecular heat transfer just beneath the surface, and cool skin is a manifestation of the temperature drop over the molecular sublayer. This also implies the existence of the viscous sublayer just beneath the surface. This, in turn, suggests that the real (physical) roughness scale of the sea surface (from below) instead corresponds to a smooth surface, which utterly contradicts the commonly accepted parameterizations.

To address these outstanding problems, the present study aims to develop a semiempirical model that would be able to describe more consistently the observed features of subsurface turbulence and wind-driven surface currents in the ocean and laboratory conditions (see sections 3 and 4). Our model development builds on the ideas of Kitaigorodskii (1984) and Terray et al. (1996) on direct injection of momentum and energy by breaking waves into a layer whose depth is on the order of the wave height. Specifically, we assume that momentum and energy losses by breaking waves can be incorporated into the momentum and turbulent kinetic energy (TKE) conservation equation for the wave-affected layer as wave-induced fluxes that attenuate with depth (the so-called body production source). Crucially, we take into account the action of all breaking waves, including usually neglected small-scale breaking (microbreaking), and incorporate into the model molecular sublayers at the sea surface (see section 5). To complement the available experimental data on the nature of surface currents and to check the model, we conducted a dedicated field experiment focused on estimation of vertical shear of the wind-driven surface currents, which is an indirect but effective way to gauge vertical distribution of turbulence (see section 2).

2. Observations of vertical shears in wind-driven currents

A series of experiments on measurements of vertical structure of wind driven current was carried out in the

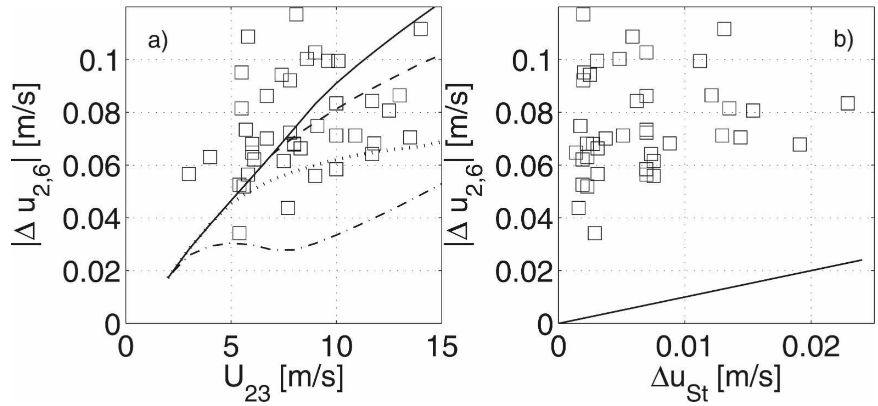

FIG. 1. (a) Magnitude of the current velocity difference between 0.5- and 5-m depths ($|\Delta \mathbf{u}_{2,6}|$) vs wind speed U_{23}. Open squares are the measurements. Curves show the model calculations for different inverse wave ages U_{23}/c_p: 1 (dashed–dotted), 2 (dotted), 3 (dashed), and 4 (solid). (b) Open squares are measurements of $|\Delta \mathbf{u}_{2,6}|$ vs quasi-Stokes velocity defined by (A.3) and estimated for observed significant wave heights and spectral peak frequencies. Solid line indicates one-to-one relation.

summer periods of 2000, 2001, and 2004 around the Marine Hydrophysical Institute (MHI) Black Sea platform (44°24′N, 33°59′E). In appendix A we describe the details of the experiment and its methodology, based on current measurements by Lagrangian drifters. Six drifters were used to estimate the current velocity $\mathbf{u}_i$ at depths $h_i = 0.25, 0.5, 1.0, 2.0, 3.0$, and 5.0 m where the drogues were located. The experiments of 2004 and 2005 were supplemented by the measurements of the velocity at the sea surface associated with drift velocity of the artificial surface slick.

a. Drifters

The experiments were performed in the range of onshore wind speeds from 3 to 14 m s^{-1}. In all cases, the surface waves represented a field of mixed seas—swell and wind waves, where the latter were normally undeveloped; as it turned out, the phase velocity of the spectral peak in all runs was approximately 3 m s^{-1} independently on wind speed (thus, inverse wave age ranged from 1.2 at lowest winds to about 4 at strongest ones). In all runs the main component of the drifter transport was due to the coastal current with velocity up to 1 m s^{-1}. To exclude this component we analyze the current velocity differences between ith and jth drifters

$$\Delta \mathbf{u}_{i,j} = \mathbf{u}_i - \mathbf{u}_j, \tag{2.1}$$

where index $i = s$ relates to the surface slick, the index i from 1 to 6 relates the drogues at 0.25, 0.5, 1, 2, 3, and 5 m, respectively. If we assume that velocity of the coastal current varies slowly over the depth range of the drogues' locations, then $\Delta \mathbf{u}_{i,j}$ corresponds to the wind-driven current in the upper layer.

Dependence of module of $\Delta \mathbf{u}_{2,6}$ (velocity difference between 0.5 and 5 m) on wind speed is shown in Fig. 1a. In the whole velocity drop between 0.5- and 5-m depths there is about 1% of wind speed, though one might conclude that it is rather wind independent. Though this result is puzzling, it is consistent with the observations by Churchill and Csanady (1983), who did not find any clear relation of relative velocity (between depths of 0.12 and 1.8 m) to the wind speed. This implies that factors other than the wind speed influence the relative velocity. Churchill and Csanady (1983) suggested the influence of the sea state on the drift velocity, and it seems that their measurements based on visual observations of the sea state support this hypothesis (see their Fig. 9).

Unlike Churchill and Csanady (1983), we also measured parameters of the surface waves. Our analysis of the data does not reveal any dependence of $\Delta \mathbf{u}_{2,6}$ on significant wave height for mixed seas or wind seas (not shown here). The other candidate could be the Stokes drift velocity. Figure 1b shows current velocity shear $\Delta \mathbf{u}_{2,6}$ against quasi-Stokes drift velocity difference between 0.5 and 5 m, calculated on the basis of (A.2) for the significant wave heights and peak frequencies of simultaneously measured wind waves. Notice that because the drifters filter out waves with wavelengths shorter than 3 m and that in all runs the wind seas' peak wavelength was about 6 m (which corresponds to the peak phase velocity 3 m s^{-1}), the tail of the wind–wave spectra should not contribute to the drifter velocity. As it follows from this figure, the relative current velocity

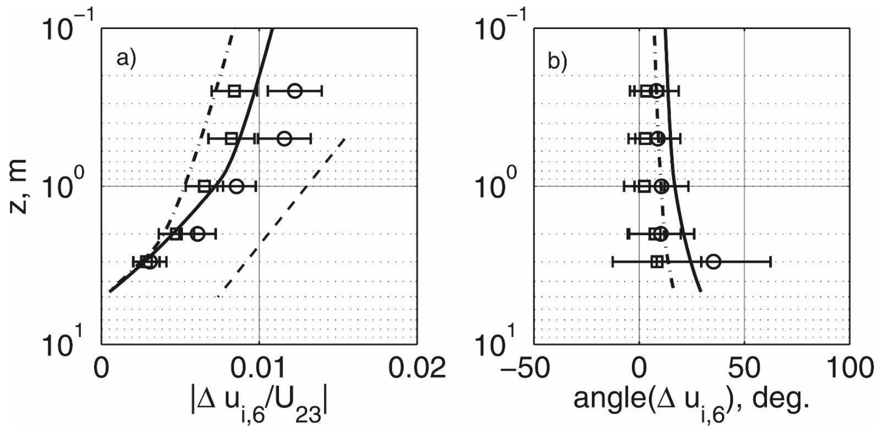

FIG. 2. Mean profiles of (a) magnitude and (b) direction of relative current velocity with respect to a 5-m depth $\Delta\mathbf{u}_{j,6}$ normalized by wind speed in the wind speed ranges U_{23} from 4 to 8 m s^{-1} (open circles) and from 8 to 12 m s^{-1} (open squares). Error bars correspond to the std dev of the data in each wind speed range. Dashed–dotted and solid lines show the model predictions for inverse wave age $U_{23}/c_p = 2$ and for wind speed 6 (solid lines) and 10 m s^{-1} (dashed–dotted lines). Dashed line indicates velocity profile $|\Delta\mathbf{u}_{j,5}|/U_{23} \propto C_D^{1/2}/\kappa \log z$, which is typical of a wall boundary layer.

does not correlate with the quasi-Stokes drift. Moreover, a remarkable feature of this comparison is that the measured current velocity difference is much larger than the expected quasi-Stokes drift caused by dominant wind waves (the solid line in this plot indicates a one-to-one relation). The similar result was found for the mixed seas as well. Thus, hereafter analyzing the data, we will neglect the impact of the quasi-Stokes drift on both the drifter velocity and vertical velocity shears.

The profiles of the relative (with respect to a 5-m depth) current velocity averaged over low and moderate wind speeds (from 4 to 8 m s^{-1} and from 8 to 12 m s^{-1}, respectively) normalized by wind speed are plotted in Fig. 2a. Bars indicate the standard deviation of the measured current velocity from the mean value in each wind speed range. At low winds, the normalized current velocity is systematically larger than at moderate winds. Note that in both cases the mean slope of the velocity profiles is less than would have been expected from the logarithmic one, which is also plotted in this figure. Profiles of direction of the relative velocity are shown in Fig. 2b. In the mean, the direction of the relative current is shifted clockwise from the wind direction. A trend of the current rotation with depth (typical of the Ekman current) is also discernable.

We introduce the nondimensional current shear vector $\mathbf{\Phi}_i$ as

$$\mathbf{\Phi}_i = \frac{\kappa z_i}{\upsilon_*}\frac{\Delta\mathbf{u}_{i,i+1}}{h_{i+1} - h_i}, \tag{2.2}$$

where $\Delta\mathbf{u}_{i,i+1}$ is the velocity difference between two successive depths, $\kappa = 0.4$ is the von Kármán constant, and υ_* is the water friction velocity. For the wall logarithmic profile, expression (2.2) reduces to $|\mathbf{\Phi}_i| = 1$. The water friction velocity was estimated from the condition of continuity of the momentum flux through the surface:

$$\upsilon_* = (\rho_a/\rho_w)^{1/2}u_*, \tag{2.3}$$

where ρ_a and ρ_w are the air and water densities, respectively, and $u_* = C_D^{1/2}U_{23}$ is the air friction velocity expressed through the wind speed U_{23} at the reference level 23 m, with the drag coefficient $C_D = \kappa^2/\ln^2(23/z_0)$ specified by the sea surface roughness scale (e.g., Smith 1988):

$$z_0 = c_1\nu_a/u_* + c_2u_*^2/g, \tag{2.4}$$

where ν_a and g are the air molecular viscosity and gravity acceleration, respectively; constants c_1 and c_2 were chosen as $c_1 = 0.12$ and $c_2 = 0.012$.

Figure 3 shows dependences of the magnitude and direction of dimensionless current velocity shear $\mathbf{\Phi}_i$ (2.2) on z, which is scaled by the Ekman boundary layer depth υ_*/f, where f is the Coriolis parameter. The estimates of $\mathbf{\Phi}_i$ are referred to as the depth $z_i = (h_{i+1} + h_i)/2$. Note that to avoid large scattering of the shear directions, only the data when the distance between successive drifters exceeded 28 m (4 lengths of the boat) are retained in Fig. 3b.

The main feature of the data in Fig. 3a is that dimensionless shears at $zf/\upsilon_* > 0.02$ exceed 1, that is, $|\mathbf{\Phi}_i| > 1$, while the data at smaller depths indicate the shears well below $|\mathbf{\Phi}_i| = 1$. We recall that our measurements

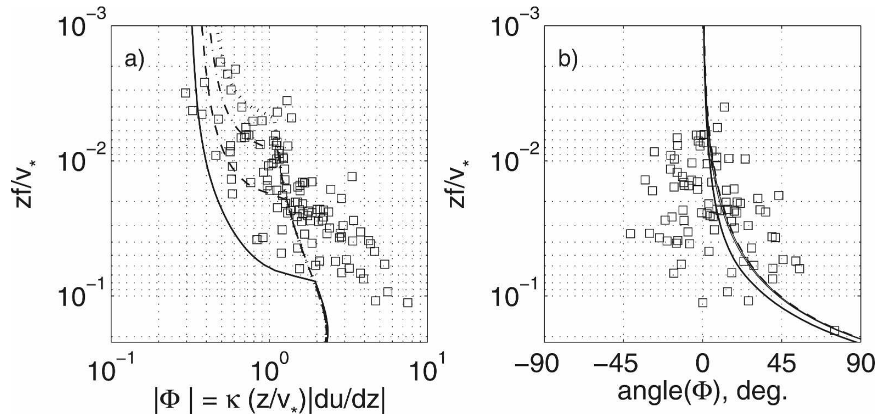

FIG. 3. (a) Magnitude and (b) direction of dimensionless current velocity shear (2.2) vs depth scaled by the Ekman boundary layer depth v_*/f. Open squares are measurements. The model predictions for wind speed $U_{23} = 10$ m s^{-1} and inverse wave ages $U_{23}/c_p = 1, 2, 3$, and 4 are shown, respectively, by solid, dashed, dashed–dotted, and dotted lines.

were performed at neutrally stratified conditions in the uppermost few meters; thus the magnitudes of velocity gradients above $|\mathbf{\Phi}_i| = 1$ may presumably be attributed to the effect of the earth's rotation. In spite of the strong scattering, a definite trend of the deviation of the current shear direction from the wind can be clearly traced in Fig. 3b. Therefore, we relate the observed high-velocity gradient at $zf/v_* > 0.02$ to the Ekman boundary layer.

At small depths, $zf/v_* < 0.02$ velocity shears are well below the value $|\mathbf{\Phi}_i| = 1$ inherent to the classical wall boundary layer. On the one hand, this observation contradicts the data presented by Csanady (1984, see his Fig. 4). On the other hand, this result is consistent with the field measurements presented in Terray et al. (1999, see their Fig. 2), characterized by low values of the current shears ($|\mathbf{\Phi}| < 1$) below the sea surface. These authors attributed the small velocity shears to the impact of enhanced turbulence mixing due to wave breaking. If we adopt (for the time being) that the turbulent eddy viscosity k_t is $k_t = \kappa z q$ (where q^2 is the scale of TKE) and also assume that in the zone of enhanced turbulence the magnitude of q as well as momentum flux are constant over depth, then the logarithmic profile of velocity should hold, $u(z) = (v_*^2/\kappa q)\ln z + \text{const}$, although with a weaker slope, which would yield

$$|\mathbf{\Phi}_i| = v_*/q. \tag{2.5}$$

In the wall boundary layer $q = v_*$ and hence $|\mathbf{\Phi}_i| = 1$. The low values of $|\mathbf{\Phi}_i|$ found in our measurements imply that TKE in the upper layer is $|\mathbf{\Phi}|^{-3}$ times enhanced in comparison with the wall turbulence. For instance, decrease of the shear in 2 to 5 times means an 8- to 125 times increase of the TKE level.

b. Slicks

Figure 4a shows the velocity difference $|\Delta\mathbf{u}_{s,2}|$ between the slick and the drifter at 0.5-m depth for various wind speeds, while Fig. 4b presents the corresponding wind drift coefficient $|\Delta\mathbf{u}_{s,2}|/U_{23}$. The number of runs with a slick is not too large; nevertheless, the wind dependence of $|\Delta\mathbf{u}_{s,2}|$ is apparent: the wind drift coefficient is approximately equal to 0.7% of the wind speed. The observed direction of the velocity difference was aligned in the mean with the wind direction (not shown here). Combining results shown in Figs. 4, 1, one may conclude that the slick drift with respect to that of a 5-m depth is in the mean about 1.7% of the wind speed. Because drift velocity at a 5-m depth is not vanishing, the absolute speed of the slick with respect to the lower boundary of the Ekman layer should be larger. However, our experimental estimate of the sea surface wind drift coefficient (identified with slick drift) seems to be smaller than the commonly accepted 3% of the wind speed [an overview of experimental estimates of the surface wind drift coefficient showing their scattering from 1%–7% can be found, e.g., in Malinovsky et al. (2007)].

Note that the data on slick drift could be used to assess the subsurface roughness scale z_{0w}. If we adopt the same assumptions as for (2.5), then an estimate of the roughness scale z_{0w} based on the slick drift velocity relatively to a 0.5-m depth is

$$z_{0w} = 0.5\exp(-\kappa|\Delta\mathbf{u}_{s,2}|q/v_*^2). \tag{2.6}$$

Such estimates of z_{0w} based on the mean slick drift coefficient ($|\Delta\mathbf{u}_{s,2}|/U_{23} \approx 0.7\%$) and the mean subsurface dimensionless current velocity shear $|\mathbf{\Phi}| \approx 0.4$

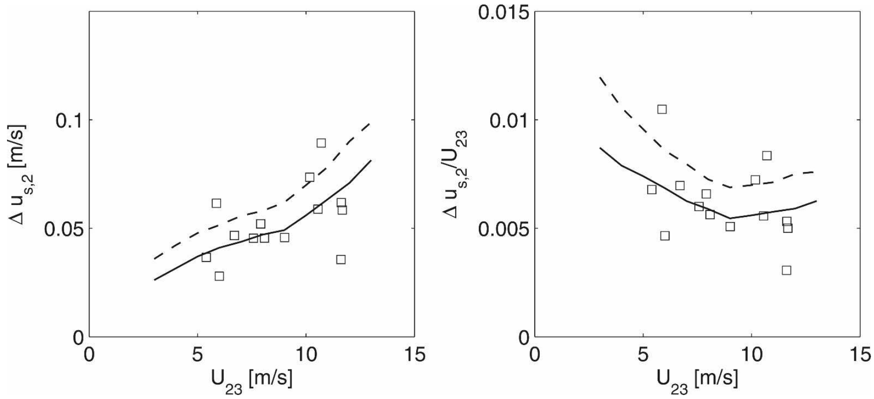

FIG. 4. (a) Velocity difference between the sea surface drift (associated with slick drift) and the drifter at 0.5-m depth vs wind speed, and (b) corresponding wind drift coefficient. Open squares are measurements. Model calculations for inverse wave ages $U_{23}/c_p = 1$ and 3 are shown by solid and dashed lines, respectively.

[which according to (2.5) is equivalent to q/v_*] gives $z_{0w} \approx 2.5 \times 10^{-3}$ m, which by two orders of magnitude exceeds the roughness scale prescribed by (2.4) for the water side of the sea surface. On the other hand, if one still retains the analogy with the wall boundary layer, then q/v_* in (2.6) is equal to one, and the roughness length is $z_{0w} \approx 6 \times 10^{-2}$ m; that is, by three orders of magnitude it exceeds prediction (2.4). Such a discrepancy is not surprising and has been mentioned in numerous studies (see, e.g., Kitaigorodskii 1994 and corresponding references). On the other hand, our estimate of z_{0w} is one order of magnitude less than the observed significant wave height, which normally serves as the sea surface roughness scale (see, e.g., Kitaigorodskii 1994; Craig and Banner 1994; Terray et al. 1999).

3. Semiempirical model

Our observations confirmed and elaborated on previous finding by Thorpe (1984), Santala (1991), and Terray et al. (1999, see also references to their Fig. 2) that shears of neutrally stratified wind-driven sea currents in the uppermost meters are significantly smaller than those expected from the wall boundary layer analogy. As was suggested on the basis of a series of field experiments (e.g., Kitaigorodskii et al. 1983; Agrawal et al. 1992; Terray et al. 1996; Drennan et al. 1996), the most plausible reason is enhanced production of turbulence due to energy losses in wind waves. At moderate and strong winds, these losses are normally associated with wave breaking.

a. An overview of basic approaches

By decomposing all dependent variables in the standard Navier–Stokes equations into mean, wave, and turbulent components as $a = \overline{a} + \tilde{a} + a'$ and applying time averaging over time scales much larger than the characteristic wave periods (we will denote such an averaging by an overbar), the assumption that these components of motion are uncorrelated enables one to obtain equations for the mean flow, with the Reynolds stresses provided by the time-averaged turbulent pulsations and wave perturbations, for the mean wave kinetic energy $E^w = \overline{\tilde{u}_i\tilde{u}_i}/2$ and TKE $q = \overline{u_i'u_i'}/2$ (for details, see, e.g., Anis and Moum 1995). In our context, the key equation describing the effect of wind waves on the water boundary layer is the TKE conservation equation, which under assumption of stationarity reads (see, e.g., Anis and Moum 1995)

$$-\partial F^t/\partial x_3 - \tau_\alpha^t \partial \overline{u}_\alpha/\partial x_3 - \overline{\tilde{\tau}_{ij}^t \partial \tilde{u}_i/\partial x_j} - \text{diss} = 0, \quad (3.1)$$

where the TKE sources–sinks are, respectively, vertical transport $\partial F^t/\partial x_3$ (F^t is the vertical flux of TKE), $\tau_\alpha^t \partial \overline{u}_\alpha/\partial x$ is the production by mean flow shear, and $\overline{\tilde{\tau}_{ij}^t \partial \tilde{u}_i/\partial x_j}$ is the production by wave-induced motions [$\tau_\alpha^t = \overline{u_a' u_3'}$ is the mean momentum flux (stress) and $\tilde{\tau}_{ij}^t$ describes wave-induced modulations of turbulent momentum flux (stress); $\overline{u}_\alpha$ and $\tilde{u}_i$ are velocities of mean flow and waves], and dissipation (diss) we do not spell out. With the use of the kinetic energy balance equation for the wave-induced motions under the same assumption of stationarity (e.g., Anis and Moum 1995; Kudryavtsev and Makin 2004),

$$-\partial F^w/\partial x_3 - \tau_\alpha^w \partial \overline{u}_\alpha/\partial x_3 + \overline{\tilde{\tau}_{ij}^t \partial \tilde{u}_i/\partial x_j} = 0, \quad (3.2)$$

the TKE balance Eq. (3.1) can be rewritten as

$$-\partial(F^t + F^w)/\partial x_3 - (\tau_\alpha^t + \tau_\alpha^w)\partial \overline{u}_\alpha/\partial x_3 - \text{diss} = 0, \quad (3.3)$$

where F^w and $\tau_\alpha^w = \overline{\tilde{u}_\alpha \tilde{u}_3}$ are the vertical fluxes of the energy and momentum of the wave-induced motions.

Existing models differ in evaluation of the role of various wave–turbulence interaction mechanisms and their parameterization.

1) EFFECT OF WAVE-INDUCED ("REGULAR") MOTIONS ON TKE

An extensive overview of the earlier works on the effect of waves breaking on the upper ocean dynamics is given in (Benilov and Ly 2002). Teixeira and Belcher (2002) developed a model for production of turbulence by wave-induced motions in the water based on the rapid distortion approach. They found that the resulting effect of waves on turbulence is similar to the TKE shear production—second term in (3.3) to which has to be added the velocity shear due to the Stokes drift. Production of turbulence results in attenuation of surface waves. However, as shown by Rascle et al. (2006), dissipation of wave energy due to production of turbulence by means of this mechanism is at least one order of magnitude weaker than the total wave energy dissipation, and thus it may be ignored as compared with direct generation of turbulence by wave breaking. Benilov and Ly (2002) introduced heuristically a turbulent diffusion of wave energy, assuming that the correlation $\overline{u_3' \tilde{u}_j \tilde{u}_j}$ between turbulent and wave-induced fluctuations does not vanish. In terms of (3.3), this hypothesis can be expressed as $F^w = -k_t \partial E^w / \partial x_3$, where E^w is kinetic energy of wave-induced motions, and k_t is turbulent eddy viscosity. As shown by Benilov and Ly (2002), this term could provide strong enhancement of TKE; however, the validity of their key assumption remains an open question.

2) SURFACE FLUX OF TKE

A more natural approach to modeling wave breaking in the upper-layer dynamics is based on introduction of the TKE flux through the sea surface, which serves as a boundary condition for the TKE balance Eq. (3.1) or (3.3) (e.g., Korotaev et al. 1976; Mellor and Yamada 1982; Craig and Banner 1994). This flux is associated with the wave energy losses, which are usually assumed to be equal or proportional to the wind energy input. The TKE flux due to wave breaking significantly exceeds the integral production of turbulence by shear current; therefore, it produces a strong enhancement of the turbulence. However [as it follows from Craig and Banner (1994) and the asymptotic analysis by Korotaev et al. (1976)], within the framework of such an approach the enhanced turbulence is confined to a very thin subsurface layer, rapidly decreasing with depth as $q \propto (z_0/z)^{0.8}$, where z_0 is a roughness scale and q is a turbulent velocity scale. At depths $z \gg z_0$ the effect of wave breaking disappears because vertical diffusion of turbulence is small compared to the TKE dissipation. This implication of such an approach is in direct contradiction to the field observations showing that the layer of enhanced turbulence is on the order of significant wave height.

To be consistent with field observations, Craig and Banner (1994) had to introduce the roughness scale of magnitude comparable with the significant wave height (H_s). Drennan et al. (1996) and Soloviev and Lukas (2003) also found that the Craig and Banner (1994) model (after a modification of the wave energy losses) is consistent with their data if the roughness scale is approximately equal to the observed H_s. Testing the same model against laboratory measurements by Cheung and Street (1988), Craig (1996) found that in the laboratory conditions the surface roughness (found by fitting the model profiles to the measured ones) is proportional to the inverse wavenumber of dominant wind waves with a proportionality coefficient ~0.4.

Thus, the seeming simplicity of accounting for wave breaking through the TKE surface flux leads to the introduction of an artificial surface roughness scale, z_0, of magnitude comparable with significant wave height. This implies that inside the roughness scale (from the real surface to z_0) both the current velocity and TKE are constant over depth. In real conditions, H_s and thus z_0 vary from 1 to 10 m. Thus, such an approach simply does not resolve the uppermost layer that is of most interest for many applications and is the subject of our study.

3) INJECTION OF ENERGY AND MOMENTUM

Inclusion of wave breaking through the boundary conditions only is also in certain contradiction with available observations. Field observations of "clouds" of air bubbles in the upper layer as well as enhanced dissipation of the TKE at depths corresponding to the significant wave heights (see, e.g., Terray et al. 1996; Melville 1996; Drennan et al. 1996; Soloviev and Lukas 2003) undoubtedly suggest that a wave-breaking event results in *a mechanical disturbance* of the upper layer over a finite depth comparable with the height of the breaking waves. Rapp and Melville (1990) and Melville et al. (2002) found in the laboratory conditions that immediate production of the turbulence extends to depths on the order of breaking-wave heights. Individual breakings create relatively long-lived turbulence beneath the water surface. This is also relevant to the small-scale breaking. As found in laboratory conditions by Zhang and Cox (1999), Siddiqui et al. (2002), Siddiqui and Loewen (2007), and Zappa et al. (2002), for example, breaking of very short waves (without visible entrainment of the air bubbles but generating parasitic capillaries) produces intense vortices just below the surface, which are classified as turbulent motions. These strong vortices disrupt the cool skin layer (i.e., the sublayer of molecular thermal conductivity) and generate a thin layer of enhanced turbulence. According to Siddiqui et al. (2002), the RMS turbulent velocities generated by microscale breaking just beneath the surface are approximately 2 times greater than at depths on the order of 1 cm. In the recent paper by Siddiqui and Loewen (2007) it was found that TKE generated by microscale breaking is significantly greater (10 times or more) than in a comparable wall layer. These measurements seem to support theoretical findings by Longuet-Higgins (1992, 1996), who showed that parasitic capillaries generated by steep, short gravity waves (microscale wave breaking) shed a strong vorticity, which together with a crest roller forms a cooperative system, or capillary roller. Energy is supplied by the gravity wave. The capillary rollers provide intensive vertical mixing, and because parasitic capillaries are a regular feature of sea surface, they should significantly affect momentum, heat, and gas transfer.

Kitaigorodskii (1984) and later Terray et al. (1996) put forward an idea that the principle source of TKE in the water boundary layer is wave breaking and that breaking directly injects both the energy and momentum to a depth on the order of the breaking-wave height. On the basis of their experimental findings, Terray et al. (1996) suggested a three-layer structure of the wave-stirred near-surface layer. The top layer (with the depth of about 60% of H_s) is a zone of direct injection of turbulence by wave breaking, and half of the total energy dissipation was found to occur there. Below this layer lies a "transition" layer (where TKE dissipation decays with depth as z^{-2}), which merges with the deeper layer where the wall boundary analogy is applicable.

The idea of direct injection of energy and momentum into the "water body" was also adopted by Sullivan et al. (2004) in their direct numerical simulation (DNS) of the upper layer driven by wave breaking. The effect of an individual breaker was modeled as a body force characterized by the breaker's strength and penetration depth. They found that action of individual breakers randomly distributed over the surface and covering just about 1.6% of its area dramatically affects the upper-layer dynamics, determining current velocity profiles, TKE, and its budget. Rascle et al. (2006) adopted some findings by Sullivan et al. (2004) to introduce the effect of breaking injection as volume sources in the TKE and momentum conservation equations. Nevertheless, in their model they retained the "magic" roughness scale on the order of H_s (originated from the TKE surface flux concept). In other words, Rascle et al. (2006) accounted for twice the effect of wave breaking—both through volume source and roughness scale. Indeed, because the volume source of TKE (proportional to the integral of spectral energy input from the wind) is mainly formed by breaking of the equilibrium range waves [see, e.g., (3.21) and (3.27b)], the roughness scale $z_0 \propto H_s$ absorbs the volume source.

b. Model approach: Momentum and energy injections by waves breaking

In the present study we will also pursue the idea of direct injection of momentum and energy by breaking waves into a layer of certain depth, which we specify later. We generalize this approach by extending it to wave breaking of all scales, including microbreaking. More specifically, we assume that each of the wave-breaking events results in local mechanical disturbances in the layer of depth z_b comparable with the breaking-wave height, feeding this layer with additional energy and momentum lost by the breaking waves.

Let $D_E(\mathbf{k})d\mathbf{k}$ and $D_{M\alpha}(\mathbf{k})d\mathbf{k}$ be the energy and momentum lost by breaking waves with wavenumbers from $\mathbf{k}$ to $\mathbf{k} + d\mathbf{k}$ in unit of time. Beneath the surface these losses are transformed into fluxes of energy dF^{wb} and momentum $d\tau^{\mathrm{wb}}$, which, as it is natural to assume, somehow attenuate over the depth interval $0 < z < z_b$ (hereafter the vertical axis is denoted by z instead of x_3); they are further turned into the turbulent kinetic energy and momentum of the mean current, respectively. As to the specific law of attenuation, notice that Sullivan et al.'s (2004) DNS modeling of the oceanic boundary layer driven by wave breaking suggests (see their Figs. 15, 17) the following picture: the wave-breaking momentum and TKE fluxes are confined to the layer $z/\lambda < 0.15$ (or $kz < 1$); they are distributed over depth approximately linearly. On this basis, we assume linear attenuation of the fluxes. Our choice of the breaker-penetration scale z_b is prompted by the laboratory study findings by Melville et al. (2002) that the breaker-penetration depth z_b is about the inverse wavenumber of breaking waves, that is, $z_b \approx 1/k$; this estimate will be used throughout our study. Thus, beneath the surface, the energy and momentum fluxes produced by the breaking of waves in a spectral band from $\mathbf{k}$ to $\mathbf{k} + d\mathbf{k}$ are

$$dF^{\mathrm{wb}}(z) = (1 - kz)D_E(\mathbf{k})d\mathbf{k}, \tag{3.4}$$

$$d\tau_\alpha^{\mathrm{wb}}(z) = (1 - kz)D_{M\alpha}(\mathbf{k})d\mathbf{k}, \tag{3.5}$$

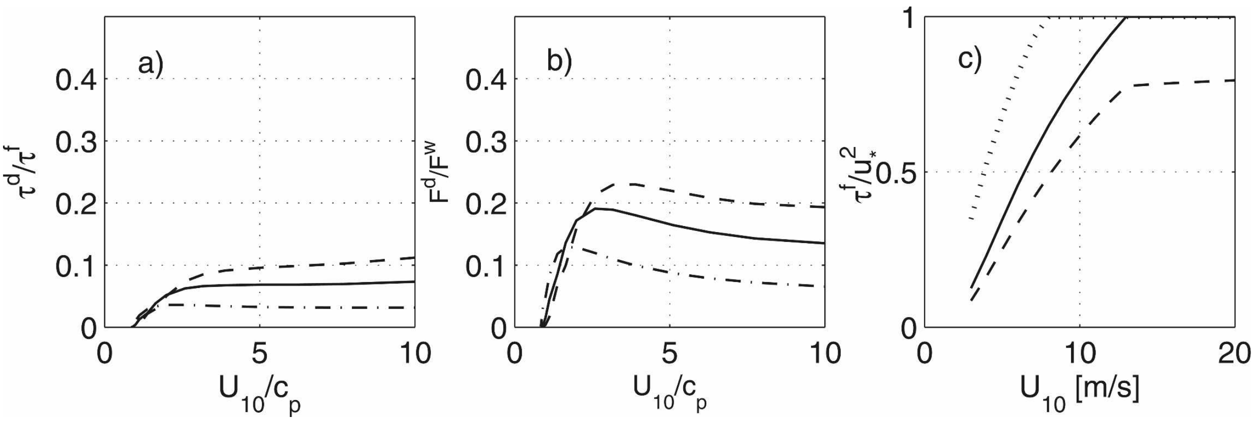

FIG. 5. Ratio of advective fluxes of (a) momentum and (b) energy specified by Eq. (B.1) to the corresponding fluxes from the wind, given by Eq. (B.2), vs inverse wave age for the wind speed 5 (dashed lines), 10 (solid lines), and 20 m s^{-1} (dashed–dotted lines). (c) The coupling parameter τ_f/u_*^2 defined by (3.23) for two values of the Charnock constant $c_2 = 0.012$ (solid line) used in the present study, and $c_2 = 0.05$ (dotted line) associated with aerodynamically rough surface at young, developing seas. Dashed line indicates surface momentum flux from breaking waves to the upper layer normalized by v_*^2—Eq. (3.26).

and they vanish at $z > k^{-1}$. Contribution of all breaking waves to TKE production and momentum at given depth z can be found by integration of (3.4) and (3.5) over $\mathbf{k}$ of all breaking waves, which reads

$$F^{\mathrm{wb}}(z) = \int_{k<1/z}^{k_b} (1 - kz)D_E(\mathbf{k})\, d\mathbf{k}, \qquad (3.6a)$$

$$\tau_\alpha^{\mathrm{wb}}(z) = \int_{k<1/z}^{k_b} (1 - kz)D_{\mathrm{M}\alpha}(\mathbf{k})\, d\mathbf{k}. \qquad (3.6b)$$

At small depths the upper limit of integration in (3.6) has to be restricted by wavenumber k_b of the shortest breaking waves, which are associated with generation of parasitic capillaries. As mentioned above, parasitic capillaries (generated by microscale breaking) and their crest roller forms a cooperative system: capillary rollers, which provide intensive vertical mixing. As established experimentally (e.g., Zhang and Cox 1999; Siddiqui et al. 2002; Siddiqui and Loewen 2007; Zappa et al. 2002), short gravity waves with wavenumber $k_g \approx 2\pi/0.05$ rad m^{-1} generate the most pronounced parasitic capillaries at wavenumber $k_{\mathrm{pc}} \approx 10^3$ rad m^{-1}. Because the phase velocities of the gravity waves and parasitic capillaries generated on their crests are approximately equal, their wavenumbers are linked as $k_g k_{\mathrm{pc}} = k_\gamma^2$, where $k_\gamma \approx 360$ rad m^{-1} is the wavenumber corresponding to the minimum of phase velocity, which separates gravity and capillary surface waves (Longuet-Higgins, 1992). Hereafter, we assume that the wavenumber of the shortest breaking (in the abovementioned sense) waves k_b producing subsurface turbulence is around $k_b \approx 2\pi/0.05$ rad m^{-1}, that is, $k_b \approx k_\gamma/3$.

c. Momentum and TKE conservation equations

In accordance with the broad physical picture we outlined, we assume that the TKE balance equation has the form (3.3), where wave-induced fluxes F^w and τ^w are replaced with the wave energy F^{wb} and momentum $\tau_\alpha^{\mathrm{wb}}$ fluxes [specified by (3.6)], which resulted from the direct injection of breaking crests into the water body

$$-\partial F^t/\partial z + P^{\mathrm{wb}} - \tau_\alpha \partial \overline{u}_\alpha/\partial z - \mathrm{diss} = 0, \qquad (3.7)$$

where $\tau_\alpha = \tau_\alpha^t + \tau_\alpha^{\mathrm{wb}}$ is the total momentum flux and $P^{\mathrm{wb}} = -\partial F^{\mathrm{wb}}/\partial z$ is the volume production of TKE by breaking injection given by [note the use of (3.6a)]

$$P^{\mathrm{wb}}(z) = \int_{k<1/z} kD_E(\mathbf{k})\, d\mathbf{k}. \qquad (3.8)$$

The total momentum flux in the water τ_α consists of the sum of wave-breaking stress $\tau_\alpha^{\mathrm{wb}}$ and classical turbulent shear stress τ_α^t; close to the surface (more specifically, at $z \ll d_E$, where d_E is the scale of the Ekman boundary layer) it is constant over depth, that is,

$$\tau_\alpha = \tau_\alpha^{\mathrm{wb}}(z) + \tau_\alpha^t(z) = \mathrm{const}. \qquad (3.9)$$

Hereafter we direct x_1 axis in the wind direction. Momentum flux in the atmospheric boundary layer $\rho_a u_*^2$ near the sea surface also splits into two parts: momentum flux to waves (form drag) τ^f and tangential surface viscous stress τ_s^ν: $\rho_a u_*^2 = \tau^f + \tau_s^\nu$. Most of the momentum flux to waves τ^f is eventually lost by wind waves due to wave breaking ($\tau_{\mathrm{diss}}^{\mathrm{wb}}$) and viscous dissipation (τ_{diss}^ν), $\tau^f = \tau_{\mathrm{diss}}^{\mathrm{wb}} + \tau_{\mathrm{diss}}^\nu$, although an a priori nonnegligible part of τ^f may also be spent on developing the wind waves (see appendix B; Fig. 5a). Thus, taking into account both momentum conservation equations in the air and in the water, the total momentum flux through the sea surface becomes

$$\tau \equiv \tau_s^\nu + (\tau_{\text{diss}}^{\text{wb}} + \tau_{\text{diss}}^\nu) = \rho_a u_*^2. \qquad (3.10a)$$

We presume that τ_{diss}^ν (which is mainly contributed by the shortest waves) can be considered as a stress acting upon the surface. Thus, the sum $\tau_s^\nu + \tau_{\text{diss}}^\nu$ in (3.10a) is an effective surface stress, which because of continuity should be equal to the momentum flux τ^t in (3.9) at the surface, that is, $\tau^t(0) = \tau_s^\nu + \tau_{\text{diss}}^\nu$. Because $\tau^{\text{wb}}(0) = \tau_{\text{diss}}^{\text{wb}}$, the unspecified yet constant in (3.9) is now determined, and the momentum conservation equation in the uppermost layer reads

$$\tau^{\text{wb}}(z) + \tau^t(z) = \rho_a u_*^2. \qquad (3.10b)$$

Taking into account the earth's rotation (Ekman boundary layer), the momentum conservation equation reads (hereafter all quantities are normalized by the water density ρ_w)

$$d(\tau^t + \tau^{\text{wb}})/dz + ifw = 0, \qquad (3.11)$$

where f is the Coriolis parameter, $w = u_1 + iu_2$ and $\tau^t = \tau_1^t + i\tau_2^t$ are complex current velocity and shear stress, and the total momentum flux $\tau = \tau^{\text{wb}} + \tau^t$ near the surface is $\tau(0) = \upsilon_*^2$ [where $\upsilon_* \equiv (\rho_a/\rho_w)^{1/2} u_*$ is the water friction velocity and τ vanishes at large depths].

To close the problem, we adopt the Kolmogorov–Prandtl closure scheme $\tau^t = -k_t dw/dz$ for turbulent momentum flux; $k_t = lq$ for turbulent eddy viscosity; and diss $= q^3/l$ for the TKE dissipation, where q is a scale of turbulence velocity and l is a turbulent mixing length, which we discuss in more detail below. Notice that the dissipation term −diss in (3.7) is written with accuracy up to a universal constant, which for the sake of simplicity is included in the scale of turbulent velocity q.

Following the standard dimensional reasoning, we may assume that the mixing length is

$$l = \kappa z \lambda(z/d_E, zk_b, \ldots), \qquad (3.12)$$

where λ is a mixing length function, which depends on the earth's rotation through the Ekman depth scale $d_E = \upsilon_*/f$, the scale of shortest breaking waves $1/k_b$ producing intensive turbulent vortices beneath the surface, and probably some other parameters affecting turbulent mixing. Mellor and Yamada (1982) and Craig and Banner (1994) reviewed existing parameterizations, arguing that in the uppermost sea layer (but well below the surface roughness scale) l should vary with depth linearly (i.e., $\lambda \approx 1$), thus $l = \kappa z$. On the other hand, aiming to include the Ekman boundary layer, one should keep in mind that in this case growth of l with z has to be halted by the earth's rotation; it implies that the mixing length function at $z/d_E \sim 1$ must asymptotically tend to $\lambda \propto d_E/z$ and $l \propto \kappa d_E$. We have chosen the following mixing length function that combines both these asymptotics (see review by Zilitinkevich and Esau 2005 and corresponding references):

$$\lambda = \left(1 + c_M \frac{z}{d_E}\right)^{-1}, \qquad (3.13)$$

where c_M is an empirical constant. Zilitinkevich and Esau (2005) estimated this constant on the basis of their large-eddy simulation of the atmospheric boundary layer as $c_M = 2.5$. Zikanov et al. (2003) investigated a water–wind-induced turbulent Ekman layer using a similar numerical method of large-eddy simulations. These authors presented their results in terms of eddy viscosity and mixing length. The constant c_M was evaluated on the basis of the data shown in Fig. 5f from Zikanov et al. (2003), which yields $c_M = 5$. We adopt this value of c_M in our study. Notice that the constant c_M also determines depth d_E of the Ekman (planetary) boundary layer: $d_E = (2\kappa/c_M)^{1/2}\upsilon_*/f$, $d_E = 0.4 \times \upsilon_*/f$ at $c_M = 5$.

As discussed above, according to the laboratory measurements, the subsurface turbulence differs dramatically from that in the wall layer. Its main feature is intensive turbulent vortices generated by microscale breaking, which sporadically disrupt the molecular surface sublayer (see, e.g., Siddiqui et al. 2002; Siddiqui and Loewen 2007; Zappa et al. 2002). Within the framework of our approach this feature could be taken into account through the mixing length prescribed by the scale of these vortices. Namely, we assume that the mixing length just beneath the surface is constant over depth $l(z) = \kappa z_b$ (where z_b is estimated as the inverse wavenumber of the shortest breaking waves, $z_b = k_b^{-1}$), and then increases linearly with depth for $z \gg z_b$. This behavior can be formalized as $l = \kappa(z + z_b)$. Such an extension of l is similar to that proposed by Riley et al. (1982) for the air side of the interface. Combining this feature with (3.13), we adopt the following parameterization of the mixing length function λ in (3.12):

$$\lambda = (1 + z_b/z)\left(1 + c_M \frac{z}{d_E}\right)^{-1}. \qquad (3.14)$$

As already discussed, at small z (but still at $z \gg z_b$) the mixing length is $l \approx \kappa z$, while at large z it is approaching a constant value $l \approx \kappa d_E/c_M = \kappa c_M^{-1}\upsilon_*/f$.

Upon making use of these closures, (3.11) and (3.7) can be rewritten as

$$\left(\frac{d^2}{d\eta^2}-\frac{d}{d\eta}\right)\hat{\tau}-i\frac{z}{\kappa\lambda d_E}\frac{\upsilon_*}{\hat{q}}\hat{\tau}=-i\frac{z}{\kappa\lambda d_E}\frac{\upsilon_*}{q}\hat{\tau}^{\mathrm{wb}},\qquad(3.15)$$

$$-(c_q/3)\lambda\hat{q}\frac{d}{d\eta}\lambda\frac{d}{d\eta}\hat{q}^3+\hat{q}^4=\hat{\tau}[\hat{\tau}-\hat{\tau}^{\mathrm{wb}}(z)] + \kappa\lambda\hat{q}z\hat{P}^{\mathrm{wb}}(z),\qquad(3.16)$$

where η is a modified vertical coordinate $\eta = \ln z$, $\hat{q} = q/\upsilon_*$; $\hat{\tau} = \hat{\tau}^{\mathrm{wb}} + \hat{\tau}^t$ is the total momentum flux including both the turbulent and wave-breaking components; the hats above momentum fluxes and rate of TKE generation by wave breaking are used to denote that these quantities are normalized by υ_*^2 and υ_*^3, respectively, and $c_q = 0.54$ is a constant involving other standard constants of the turbulent closure scheme. To derive (3.15), we have differentiated (3.11) with respect to z. As discussed above [see (3.10)], the solution of (3.15) at small z must obey

$$\begin{cases}\hat{\tau}=1, & \text{if}\quad \eta\to-\infty\\ \hat{\tau}=0, & \text{if}\quad \eta\to\infty\end{cases}.\qquad(3.17)$$

The first term in the lhs of (3.16) describes vertical diffusion of TKE by turbulence. We may anticipate that this term, as well as in the classical wall boundary layer, may be also ignored in the wave-stirred layer. To justify this suggestion, let us consider the "log-part" of the wave-stirred layer, so that in (3.16) $\lambda = 1$, and the shear production (first term in the rhs) is ignored with respect to production of TKE by wave breaking. Then (3.16) is reduced to a linear ordinary differential equation relative to $\hat{q}^3$ obeying the boundary conditions $d\hat{q}^3/d\eta = 0$ at the surface $z = z_0$ and at a lower boundary, $z = z_h$ (turbulence is produced by volume source, therefore there is no TKE flux through the surface). Taking into account these boundary conditions, the complete integral of the truncated differential Eq. (3.16) reads

$$\hat{q}^3=\int_{z_0}^{z_h}G(z,z_1)\kappa z_1\hat{P}^{\mathrm{wb}}(z_1)\,d\ln z_1,\qquad(3.18)$$

where $G(z, z_1)$ is the Green function: $G(z, z_1) \propto (z_1/z)^m$ if $z_1 < z$ and $G(z, z_1) \propto (z_1/z)^{-m}$ if $z_1 > z$ satisfying the conditions $\int_{z_0}^{z_h} G(z, z_1)d\ln z_1 = 1$, where $m = (3/c_q)^{1/2} \approx 2.4$. Within the framework of our model, injection of turbulence by breaking waves of various scales is spread over the entire depth of the wave-stirred layer, and inside this layer the volume source of turbulence $z\hat{P}^{\mathrm{wb}}$ varies with depth as $z\hat{P}^{\mathrm{wb}} \propto z^{1/2}$ [see (3.27b)]. Because $z\hat{P}^{\mathrm{wb}}$ varies with depth slower than the Green function (its exponent is $\pm m$), we may expand $z\hat{P}^{\mathrm{wb}}$ in the Taylor series, and the first- order solution (3.18) can be approximately written as $\hat{q}^3 \approx \kappa z\hat{P}^{\mathrm{wb}}(z)\{1 - m/[2(m^2 - 1)]\}$. Thus, we can conclude that up to $O[1/(2m)] \approx 20\%$ accuracy, the wave-breaking production is balanced by dissipation, and diffusion does not play any important physical role in the wave-stirred layer. However, at its low boundary, where a sharp gradient of wave-breaking source may exist, the diffusive term can dominate the TKE balance. We neglect the existence of the diffusion layer and match the solutions in the wave-stirred and sheared layers, ignoring the details of the structure of the diffusion layer. Thus, hereafter, the first term in the lhs of (3.16) is ignored.

d. *Parameterization of TKE production and momentum flux due to wave breaking*

To solve (3.15) and (3.16) we need to find $\hat{\tau}^{\mathrm{wb}}$ and $\hat{P}^{\mathrm{wb}}$, which are integrals of the corresponding spectral momentum and energy dissipation due to wave breaking. In spite of extensive experimental and theoretical efforts of different groups of investigators, the spectral form for the wave energy dissipation is not known yet, and various parameterizations have been suggested to advance wind–wave-related problems. In particular, Phillips (1985) argued that in the equilibrium range of the wave spectrum, the energy dissipation $D_E(\mathbf{k})$ is proportional to the wind energy input (I_W), that is, $D_E(\mathbf{k}) \propto I_W(\mathbf{k})$. However, this hypothesis is not appropriate in the vicinity of the spectral peak, especially when wind seas are developing. All the studies concerned with the effect of wave breaking on the upper ocean turbulence have presumed that energy input from wind is exactly balanced by the energy losses due to wave breaking (e.g., Craig and Banner 1994; Terray et al. 1996; Drennan et al. 1996; Rascle et al. 2006). The momentum fluxes above and beneath the sea surface are also commonly assumed to be equal. This oversimplification of the problem might lead to some discrepancies with reality, especially for young seas' conditions, when a fair portion of momentum and energy fluxes coming from the wind could be spent on development of the wave field.

In appendix B we estimate the share of the energy and momentum fluxes spent on the wave field development (F^d and τ^d, respectively) with respect to the energy F^w and momentum τ^f fluxes coming from the wind. Ratios τ^d/τ^f and F^d/F^w as a function of inverse wave age U_{10}/c_p for wind speeds 5, 10, and 20 m s^{-1} are shown in Figs. 5a,b. Momentum flux spent on development of the wave field is about one order of magnitude smaller than the wind momentum flux to waves; thus further on we neglect τ^d, assuming that momentum flux from wind is balanced by momentum losses through wave breaking and viscous dissipation. In contrast to τ^d, the relative role of advective energy flux with respect to the wind forcing is more significant. As follows from

Fig. 5b, at low wind speed, magnitude F^d/F^w attains 25% and decreases with increasing wind speed. Thus models aspiring to describe wind–wave-surface current interaction with an accuracy exceeding 25% have to take finite F^d into account. This could be done by assuming that energy dissipation due to wave-breaking F^{wb} relates to wind energy forcing as $F^{\mathrm{wb}} = F^w(1 - \Delta)$, where $\Delta = F^d/F^w$. However, because a number of studies already made bold assumptions, our aspirations are more modest, and further on, for simplicity we also neglect F^d, assuming that $F^{\mathrm{wb}} = F^w$ at any stage of wave field development. Notice that the problem nevertheless is strongly dependent on wave age through F^w and depth of momentum and energy injection [see Eqs. (3.26) and (3.27b)].

The specific spectral distribution of the losses F^{wb} and τ^{wb} is still an open question. However, because F^{wb} and τ^{wb} are not strongly dependent on wave age, and thus the major part of these quantities is supported by the equilibrium range, for the absence of better alternatives, we adopt in the present study Phillips's (1985) hypothesis; that is, we assume the spectral distribution of F^{wb} and τ^{wb} to be similar to the corresponding wind input:

$$D_M(\mathbf{k}) = \beta k \cos\varphi E(\mathbf{k}) d\mathbf{k}$$
$$D_E(\mathbf{k}) = \beta\omega E(\mathbf{k}) d\mathbf{k}, \tag{3.19}$$

where we took into account that $M_\alpha(\mathbf{k}) = (k_\alpha/\omega)E(\mathbf{k})$ and that $\beta = c_\beta(u_*/c)^2\cos^2\varphi$ is the wind–wave growth rate. Experimental evidence supporting Phillips's (1985) hypothesis was provided by Melville and Matusov (2002). By definition, the wave energy spectrum $E(\mathbf{k})$ is linked to the saturation spectrum $B(\mathbf{k})$ as $E(\mathbf{k}) = \rho_w g k^{-4} B(\mathbf{k})$. In turn, the saturation spectrum can be written as $B(\mathbf{k}) \equiv B(k)A_B(\varphi, k)$, where $B(k)$ is the omnidirectional spectrum and $A_B(\varphi, k)$ is its angular spreading. Then the wave breaking momentum flux (3.6b) and TKE production (3.8) normalized by v_*^2 and v_*^3 can be rewritten as

$$\hat{\tau}^{wb}(z) = c_*(\rho_w/\rho_a)\int_{k<\min(1/z,k_b)}(1 - kz)B_o(k)A_B^\tau(k)\, d\ln k, \tag{3.20}$$

$$\hat{P}^{wb}(z) = c_*(\rho_w/\rho_a)^{3/2}\int_{k<\min(1/z,k_b)} k(c/u_*)B_o(k)A_B^P(k)\, d\ln k, \tag{3.21}$$

where $B_o(k) = B(k)/c_B$ is the omnidirectional saturation spectrum normalized by its saturation constant c_B [therefore $B_o(k)$ is a universal shape of the saturation spectrum]; $A_B^\tau = \int A_B(\varphi, k)\cos^2\varphi|\cos\varphi|\, d\varphi$ and $A_B^P = \int A_B(\varphi, k)\cos\varphi|\cos\varphi|\, d\varphi$ are integrated over φ angular distribution of momentum and energy wind input; c_* is a constant that represents a product of saturation and growth-rate constants $c_* = c_\beta c_B$.

To complete our parameterization we need to specify the shape of the saturation spectrum and the constant c_*. Because the depth of a breaker penetration is $\sim 1/k_b$, the former controls vertical distribution of wave-breaking stirring, while the latter determines the magnitude and significance of the effect. Therefore, the choice of c_* is important and has to be discussed in detail.

First we note that the same constant determines the form drag of the sea surface from the air side. As discussed in section 3.2, the momentum conservation equation in the atmospheric boundary layer integrated over height reads $\rho_a u_*^2 = \tau^f + \tau_\nu^s$. Therefore, momentum flux to waves normalized by $\rho_a u_*^2$ is $\tau^f/\rho_a u_*^2 = 1 - \tau_\nu^s/\rho_a u_*^2$. Following Kudryavtsev and Makin (2001), the viscous surface stress τ_ν^s is expressed as

$$\tau_\nu^s/\rho_a u_*^2 = 1/(\kappa c_\nu)\ln(\delta_\nu/z_0), \tag{3.22}$$

where $\delta_\nu = c_\nu \nu_a/u_*$ is the viscous sublayer thickness, $c_\nu \approx 10$, z_0 is the surface roughness scale, and ν_a is the air molecular viscosity. Kudryavtsev and Makin (2001) treated z_0 as a solution of the wind-over-wave coupling problem. Implementation of such an approach is out of the scope of the present study. In our context, we have already prescribed z_0 by (2.4), and we will use this relation further on, relying on the fact that it fits "well" the observed aerodynamic roughness of the sea surface. Then employing (2.4), the contribution of the form drag to the total surface drag (the so-called coupling parameter) is estimated as

$$\tau^f/\rho_a u_*^2 = 1 - \frac{1}{\kappa c_\nu}\ln\left(\frac{c_\nu}{c_1 + c_2 u_*^3/(\nu_a g)}\right), \tag{3.23}$$

where c_1 and c_2 are the roughness scale constants in (2.4). Transition from the aerodynamically smooth surface (when form drag vanishes) to the rough one (when surface drag is mostly provided by momentum flux to waves) is controlled by the second term in (3.23). Notice that the Charnock constant c_2 in (3.23) could be a function of either wind speed or wave age. By definition, $\tau^f/\rho_a u_*^2$ specified by (3.23) has to be confined within $\tau^f/\rho_a u_*^2 \le 1$. Figure 5c shows contribution of the form drag to the total drag (coupling parameter) at two values of the Charnock constant: $c_2 = 1.2 \times 10^{-2}$ (used in the present study) and $c_2 = 5 \times 10^{-2}$ considered as an upper limit for the Charnock constant, which presumably may be attained in young, developing seas. Estimates of the coupling parameter (3.23) shown in this figure are similar to those found by Kudryavtsev and Makin (2001) from a rather sophisticated wind-over-wave coupling model.

Because all the constants in (3.23) had already been established empirically, this equation can be used to assess the model constant c_*. According to our assumptions, the expression for the momentum flux at the surface (from the air side) is similar to (3.6) at $z = 0$, where, however, the upper limit of integration (instead of the shortest breaking wave scale) must be extended over all short waves supporting momentum flux:

$$c_*(\rho_w/\rho_a)\int_k A_B^\tau B_o(k)\, d\ln k = 1 - \frac{1}{\kappa d_\nu}\ln\left(\frac{c_\nu}{c_1 + c_2 u_*^3/(\nu_a g)}\right). \quad (3.24)$$

This equation links the description of the sea surface [in terms of the saturation spectrum $B(k)$], its interaction with the airflow, and feeding the upper layer with momentum and TKE via wave breaking.

In the present study, for the sake of simplicity, we use the simplest shape of the saturation spectrum (Phillips 1977): $B_o(k) = 1$ at $k_p < k < k_{\rm pc}$ and $A_B(\varphi) = 1/2(\cos\varphi)$ at $-\pi/2 < \varphi < \pi/2$, where $k_{\rm pc}$ is a high-frequency cutoff of the spectrum. We assume this cutoff to be related to the parasitic capillaries generated by the shortest breaking waves with $k = k_b$. Because wavenumbers of parasitic capillaries generated by gravity waves are linked as $k_b k_{\rm pc} = k_\gamma^2 \equiv g/\gamma$ (Longuet-Higgins 1992), and we have already assumed that $k_b = k_\gamma/3$, then the high-wavenumber cutoff is $k_{\rm pc} = 3k_\gamma$. Then the estimate of the model constant c_* defined by (3.24) for the fully developed seas and totally rough surface (when the rhs in (3.24) equals one) yields $c_* \approx 2.4 \times 10^{-4}$. As an example, this value of c_* at the growth-rate constant $c_\beta = 4 \times 10^{-2}$ (Plant 1982) gives the saturation constant $c_B = 6 \times 10^{-3}$, which is consistent with the expected value (Phillips 1977). Notice that the parameterization of the spectrum adopted here may not be entirely appropriate for the fetch-limited conditions typically found in the laboratory, when the overshoot effect dominates the spectral peak shape and its level, and thus momentum and energy losses defined by (3.20) and (3.21). To apply the model to such conditions, one has to use the Joint North Sea Wave Project (JONSWAP)-type wave spectra rather than the simplest parameterization.

For the chosen wave-spectrum model, momentum flux (3.20) and rate of production of TKE (3.21) due to wave breaking are

$$\hat{\tau}^{\rm wb}(z) = c_\tau^{\rm wb} T(z/z_p), \quad (3.25)$$

$$\hat{P}^{\rm wb}(z) = \alpha^{-1} c_P^{\rm wb} P(z/z_p), \quad (3.26)$$

where $c_\tau^{\rm wb}$ and $c_P^{\rm wb}$ are constants expressed through other models' constants: $c_\tau^{\rm wb} = c_* A_B^\tau(\rho_w/\rho_a)$ and $c_P^{\rm wb} = 2c_* A_B^P C_d^{-1/2}(\rho_w/\rho_a)^{3/2}$; $\alpha = U_{10}/c_p$ is the inverse wave age; C_d is the drag coefficient; and $T(z/z_p)$ and $P(z/z_p)$ are universal profile functions

$$T(z/z_p) = \ln(z_p/z') + z/z_p(1 - z_p/z'), \quad (3.27a)$$

$$P(z/z_p) = (z' z_p)^{-1/2}[1 - (z'/z_p)^{1/2}], \quad (3.27b)$$

where $z' = \max(z_b, z)$, and $z_b = 1/k_b$ and $z_p = 1/k_p$ are the depths of injection of energy and momentum by shortest and longest breaking waves into the upper layer. The profile functions $T(z/z_p)$ and $P(z/z_p)$ are equal to zero for $z > z_p$. Integral of $\hat{P}^{\rm wb}$ over all depths corresponds to the wave-breaking energy flux at the sea surface. For developed seas ($\alpha = 1$) this integral is $\int \hat{P}^{\rm wb} dz \approx c_P^{\rm wb} = 1.7 \times 10^2$, which is consistent with the constant adopted by Craig and Banner (1994) and Craig (1996).

Figure 5c shows momentum flux from breaking waves at the sea surface [as given by (3.25) at $z = 0$]. According to our model predictions, the portion of the total momentum transported by wave breaking increases with wind speed, and at wind speeds above 13 m s^{-1}, wave breaking provides about 80% of the total momentum coming from the wind into the upper layer.

4. Model predictions and comparison with observations

a. Model predictions

It is easy to see that the TKE Eq. (3.16) (where, to remind, the first term in the lhs has been ignored) has approximate solutions corresponding to the limits when the TKE production is dominated by either shear stress,

$$\hat{q}(z) \approx [\hat{\tau}(\hat{\tau} - \hat{\tau}^{\rm wb})]^{1/4},$$

or wave breaking,

$$\hat{q}(z) \approx (\kappa z \lambda \hat{P}^{\rm wb})^{1/3}.$$

There is no obvious way to find a uniformly valid solution to (3.16) and the exact formulas are too bulky to be of practical value; however, remarkably, a superposition of the two above solutions of (3.16) in the form

$$\hat{q}(z) = \{[\hat{\tau}(\hat{\tau} - \hat{\tau}^{\rm wb})]^{3/4} + \kappa z \lambda \hat{P}^{\rm wb}\}^{1/3} \quad (4.1)$$

uniformly approximates the exact solution with the error not exceeding 3%, which was established by comparing (4.1) with the numerical solution for a wide

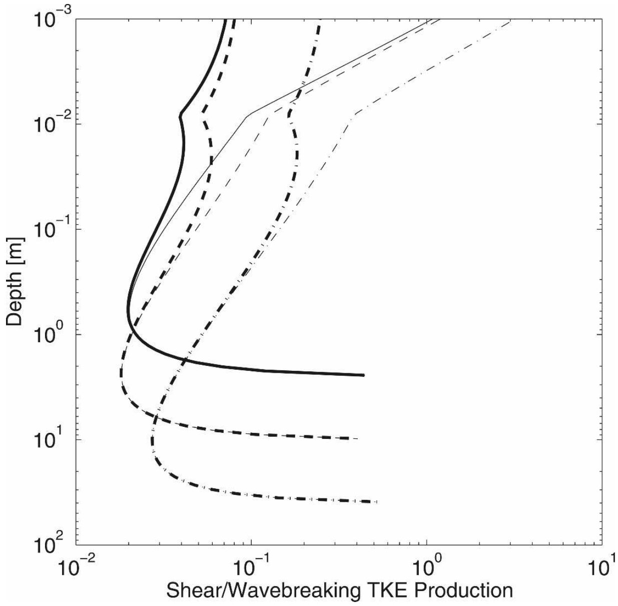

FIG. 6. Ratio of the TKE shear production [first term in rhs of (3.16)] to the wave-breaking production [second term in rhs of (3.16)] vs depth at wind speeds 5 (solid line), 10 (dashed line), and 20 m s^{-1} (dashed–dotted line). Thin lines correspond to the mixing length function (3.14) when parameter z_b vanishes (mixing length decreases continually toward the surface).

range of parameters. This accuracy is sufficient for our purposes, and later we will rely on approximation (4.1).

Relation (4.1) and the momentum conservation Eq. (3.15) represent a coupled system that can easily be solved numerically by iterations with boundary conditions (3.17). Once $\hat{\tau}$ and q are found, finding velocity shear is straightforward:

$$\frac{dw}{dz} = \frac{\upsilon_*}{\kappa z}\frac{\hat{\tau} - \hat{\tau}^{\mathrm{wb}}}{\hat{q}\lambda}, \tag{4.2}$$

where w is the complex velocity. At a small depth, $z \ll d_E$ mixing length function is $\lambda \approx 1$, and the solution of (3.15) is $\hat{\tau} \approx 1$. If the effect of wave breaking is negligible (i.e., $\hat{q} \approx 1$ and $\hat{\tau}^{\mathrm{wb}} \ll 1$), the Eq. (4.2) reduces to the shear in the logarithmic velocity profile typical of wall turbulence. On the contrary, if the generation of turbulence by wave breaking is much stronger than shear production (i.e., $\hat{q} \gg 1$), then velocity shear (4.2) is much weaker than could have been expected from the wall boundary layer analogy.

Figure 6 shows the ratio of turbulence shear production [first term on the rhs of (3.16)] to the wave-breaking production [second term on the rhs of (3.16)] at wind speeds of 5, 10, and 20 m s^{-1} and developed seas ($\alpha = 1$). As follows from this figure, at depths of $z < 1/k_p$, shear production is much weaker than the wave-breaking one at all wind speeds. Notice that in the upper layer the relative role of wave-breaking production decreases with the wind. The explanation is that the depth of penetration of the TKE generation by wave breaking expands with increasing wind speed, which in turn results in a decrease of the TKE production: $\hat{P}^{\mathrm{wb}}(z) \propto (g/zu_{10}^2)^{1/2}$ [see (3.27b)]. If we assume that the mixing length decreases linearly toward the surface [i.e., in (3.14), the term z_b/z disappears, and thus there is no imposed mixing length scale related to the microscale breaking], then the relative role of wave-breaking production [which at $z < z_b$ is constant over depth; see (3.27b)] is weakening at a small depth, as shown by thin lines in Fig. 6. Then the decreasing role of wave breaking leads to a restoring of the wall boundary just beneath the surface, which contradicts both the common sense and available laboratory observations (Siddiqui et al. 2002; Siddiqui and Loewen 2007; Zappa et al. 2002). Thus, hereafter, all model calculations will be performed with the mixing length function given by (3.14).

As an example, vertical distributions of the dissipation $\varepsilon = q^3/(\kappa z\lambda)$ as predicted by the model at wind speed 10 m s^{-1} and various wave ages are shown in Fig. 7. Figures 7a,b present model ε using the wall boundary layer scaling ($\upsilon_*^3/\kappa z$ for dissipation rate, and υ_*^2/g for z) while Figs. 7c,d employ the scaling proposed by Terray et al. (1996) and Drennan et al. (1996). Figures 7a,c relate to the logarithmic boundary layer when the effect of the earth's rotation is ignored [then in (4.1) $\tau = 1$ and $\lambda = 1$]; Figs. 7b,d show the results of calculations based on the full Ekman model.

As follows from the figure, the dissipation for developed seas exceeds by 20 times the values expected in the wall boundary layer (Fig. 7a), and the zone of the most enhanced dissipation is located at a depth on the order of $gz/\upsilon_*^2 \propto 10^5$. For young seas, the TKE dissipation is smaller and the depth of its maximum shifts toward the surface. Qualitatively, this result is consistent with the data presented by Anis and Moum (1995, their Fig. 4) and Drennan et al. (1996, their Fig. 4). Dependence of the TKE dissipation on wave age could explain the strong scattering of the data plotted in the wall layer coordinates. Terray et al. (1996) and Drennan et al. (1996) revealed that scaling of ε by F^w/H_s and depth by H_s (where F^w is wind energy input to all waves and H_s is significant wave height) collapses the collected data (Terray et al. 1996, their Fig. 7; Drennan et al. 1996, their Fig. 5). The same model calculations as in Fig. 7a, but scaled by F^w/H_s and H_s, are shown in Fig. 7b. Besides the large depths, the models' predictions for different wave ages collapse (the same was also found for other wind speeds, not shown here). Because pro-

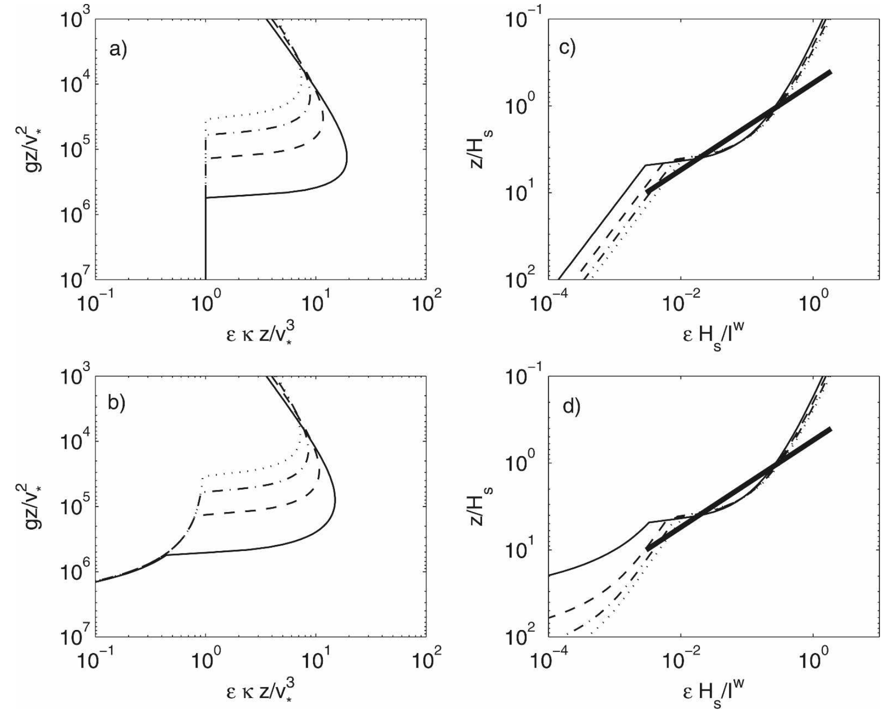

FIG. 7. Normalized dissipation rate as predicted by the model vs dimensionless depth at wind speed 10 m s^{-1} for different inverse wave ages U_{23}/c_p = 1 (solid lines), = 2 (dashed lines), = 3 (dashed–dotted lines), and = 4 (dotted lines). (a), (b) Wall boundary layer scaling: $\varepsilon\kappa z/\upsilon_*^3$ vs $z\upsilon_*^2/g$. (c), (d) Wind–wave scaling: $\varepsilon H_s/F^w$ vs z/H_s. Model calculations shown in (b) and (d) take into account the earth's rotation (the Ekman boundary layer). Bold solid lines in (c) and (d) are empirical relation $\varepsilon H_s/F^w = 0.3(z/H_s)^{-2}$ proposed by Terray et al. (1996).

duction of turbulence is dominated by wave breaking (see Fig. 6) and vertical distribution of $\hat{P}^{\mathrm{wb}}$ depends on a depth scaled by k_p and $\int P^{\mathrm{wb}}\,dz = F^w$, scaling of ε and z by F^w/H_s and H_s leads to a universal law.

The full solution of the problem is found by numerical integration of (3.15) supplemented by (4.1) and boundary conditions (3.17). Results of calculations taking into account the earth's rotation are shown in Figs. 7b,d. The earth's rotation affects the current shears and thus shear production of TKE in the Ekman layer at $z > k_p^{-1}$, where the source of TKE generation by wave breaking does not penetrate and where velocity shears are weakening with the depth. Thick lines in Figs. 7c,d show empirical dependences proposed by Terray et al. (1996) and Drennan et al. (1996): $\varepsilon H_s/F^w = 0.3(z/H_s)^{-2}$. On the whole, the model is consistent with their empirical relation, demonstrating the same level of dissipation.

Figure 8 shows an example of model profiles for the current velocity, the turbulent eddy viscosity coefficient, and the turbulent velocity scale at a wind speed of 10 m s^{-1} and fully developed seas. Overall, the shape of velocity profile possesses the features typical of the Ekman current: in the surface layer, current velocity deviates clockwise from the wind vector, and it continues to rotate clockwise at larger depths. Due to enhanced turbulent mixing caused by wave breaking, vertical distribution of the current velocity in the uppermost layer is almost uniform; at the depths $zf/\upsilon_* < 4 \times 10^{-2}$, which presumably belong to the log-boundary layer (remember that in our model the Ekman layer depth is $d_E = 0.4\upsilon_*/f$), the velocity gradient is much smaller than would be expected from the wall boundary layer (shown by thin solid line). Turbulent eddy viscosity k_t scaled by the wall boundary layer one, $k_t/\kappa\upsilon_* z \equiv \hat{q}\lambda$, is shown in Fig. 8b). In the log-boundary layer (except in the uppermost part) turbulent mixing exceeds by 2–3 times the wall boundary layer prediction. This is, again, due to the effect of wave breaking, which enhances both TKE (the scale of the TKE velocity is also shown) and turbulent mixing. A rapid growth of eddy viscosity toward the surface reflects enhanced turbulent mixing by microscale breaking, which is parameterized in our model through the mixing length function (3.14). Effect of the earth's rotation below the wave-stirred layer restrains velocity shears and thus production of turbulence and turbulent mixing, which explains rapid attenuation of the TKE and eddy viscosity at $zf/\upsilon_* \propto 1$.

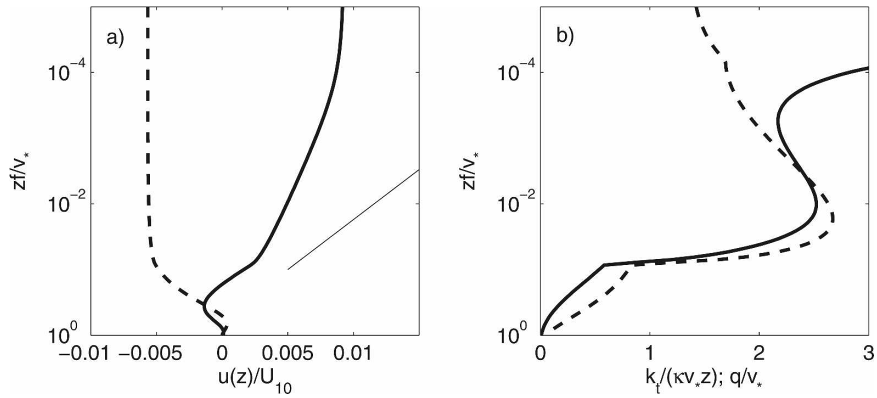

FIG. 8. (a) Profiles of current velocity u/U_{10} (solid line) and v/U_{10} (dashed line) components scaled by wind speed. Thin solid line indicates velocity profile in the wall boundary layer: $u/U_{10} \propto \cos\varphi_s(C_d\rho_a/\rho_w)^{1/2}\ln(zf/v_*) + \text{const}$, where φ_s is direction of the surface drift. (b) Profiles of turbulent eddy viscosity $k_t/\kappa v_* z$ (solid line) scaled by wall boundary layer prediction, and TKE velocity scale q/v_* (dashed line) scaled by water friction velocity.

Figure 9 shows the magnitude of the surface drift velocity and its direction for different wave ages of wind seas. Notice that here by the term *surface*, we mean the depth just below the viscous sublayer (the latter is the subject of special consideration in section 5.) For developed seas, the drift coefficient is about 1.2% of wind speed and slightly increases with wind for wind speeds exceeding 10 m s^{-1}. In the case of developing seas, the surface drift coefficient is higher, and it increases for younger wind waves, because enhancement of turbulence by wave breaking is confined to smaller depths. Therefore, the wave-stirred layer thickness is smaller, while the wall boundary layer is expanding, which leads to larger shears and to an increase of the surface drift. Our estimates of the surface drift coefficient are lower than the commonly accepted 3% that are supported by observations.

b. The drifter experiment

The model predictions of the current velocity difference between 0.5 and 5 m are compared in Fig. 1 with the drifter measurements. The calculations were performed for the inverse wave ages U_{23}/c_p = 1, 2, 3, and 4, which cover the range of U_{23}/c_p in the experiment. The model current velocity drop is strongly wave-age dependent. Overall, the model predictions are inside the cloud of the measurements, though an underestimate of $|\Delta\mathbf{u}_{2,6}|$ by the model is also revealed.

Normalized (by wind speed) profiles of a velocity defect with respect to 5 m at wind speeds of 6 and 10 m s^{-1} are shown in Fig. 2 for the wind seas of inverse wave age $U_{23}/c_p = 2$. In agreement with the experiment, the model predicts a decrease of the normalized current velocity with an increase of wind speed. There are two

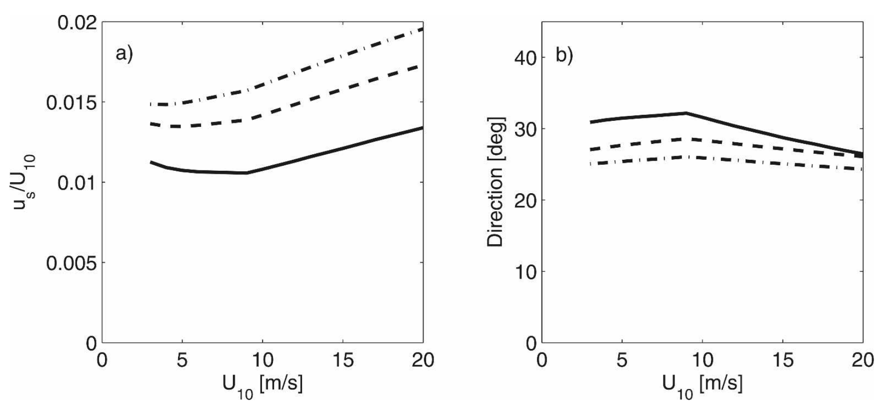

FIG. 9. (a) Magnitudes and (b) directions of the sea surface drift for different wave ages: U_{10}/c_p = 1 (solid), = 2 (dashed), and = 3 (dashed–dotted lines).

likely mechanisms explaining this tendency: first, an increasing portion of the momentum flux is provided by wave breaking, which leads to a relative suppression of the turbulent stress and thus the current velocity [see (4.2)]; second, a deeper penetration of enhanced turbulence (with $\hat{q} > 1$) according to (4.2) leads to a weakening of the current velocity shears in a deeper layer with the increase of wind. Notice that similar to Fig. 1, the model profiles in Fig. 2 underestimate the observed velocity defect, though agreement between the model and the observed current velocity directions is quite good.

Figure 3 compares the data with the model dimensionless velocity shear

$$|\mathbf{\Phi}| \equiv (\kappa z/v_*)du/dz = (\hat{\tau} - \hat{\tau}^{\mathrm{wb}})/\hat{q}\lambda$$

[see (4.2)] as a function of normalized depth zf/v_* for inverse wave ages $U_{23}/c_p = 1$, 2, 3, and 4 and a wind speed of 10 m s^{-1}. Because the depth of penetration of TKE production by wave breaking is determined by the spectral peak wavenumber, velocity shears are strongly dependent on wave age. Enhanced generation of turbulence by wave breaking explains observed low values of velocity shear beneath the surface, $|\mathbf{\Phi}| \approx 0.2 \ldots 0.4$, which is much less than in the wall boundary layer. In the Ekman part of the boundary layer, at $zf/v_* > 2 \times 10^{-2}$, the velocity gradient predicted by the model exceeds the value $|\mathbf{\Phi}| = 1$, but at these depths the model noticeably underestimates observed shears. The reason is not clear. Though we controlled the upper layer stratification and selected only the data related to the neutral one, some small temperature gradient in the Ekman layer could have affected the turbulence and thus velocity shears (remember that experiments were performed in the daytime under conditions of strong solar heating of the upper layer). The other plausible reason is contribution of the vertical shears in the coastal current, which (contrary to our expectations) turned out to be not negligible. Also notice that the model can be easily fitted to the data in the Ekman part in Fig. 5 via a 10-times increase of the mixing length parameter c_M in (3.14). However, such a model tuning is meaningless, because the order of magnitude of this constant, found in the large-eddy simulations, seems to be quite reliable.

It is also worth noticing that in our observations, as mentioned in section 2, the "background" velocity of the coastal current reached 1 m s^{-1}. Therefore, one may anticipate that wind waves traveling through the current from the open sea to the area of drifter observations could be affected by wave–current interaction. Although we did not observed visually any surface signatures of such an interaction (like an area of enhanced or suppressed roughness), we cannot rule out that our observations are somehow affected by a coastal current. However, because we didn't trace the spatial variations of the current and wave field, this effect is not taken into account in the model nor in the model comparison. Note that an inhomogeneity of the background current can be easily incorporated within the framework of the present model; we just have to take into account the effect of current velocity gradients on the energy and momentum gains and losses in (3.6) and (3.19). Wave breaking is very sensitive to the presence of surface current gradients and is strongly enhanced–suppressed in the zones of surface current convergence–divergence (quantitative estimates of impact of some kind of surface currents on wave breaking can be found in Kudryavtsev et al.2005). Thus, at a given wind speed, subsurface turbulence and wind-driven current could also be affected by background (not wind driven) surface currents through wave energy and wave-breaking modulation due to wave–current interaction. Further discussion of this problem is out of the scope of the present study.

5. Current velocity profiles beneath the sea surface

a. Viscous sublayer

We assume that from the top, the sea surface is "covered" by a water molecular sublayer. Though the sea surface is sporadically disrupted by wave breaking (see, e.g., Siddiqui et al. 2002; Siddiqui and Loewen 2007), the molecular sublayer recovers rapidly. In the mean, the molecular sublayer should certainly exist, at least up to very strong winds, when wave-breaking foam becomes the dominant feature of the water surface. Just beneath the surface, the molecular diffusion transports both momentum and heat. The manifestation of the molecular sublayer at the water side of the sea surface as a cool temperature skin is a well-known fact and a routinely observed phenomenon (e.g., Sounders 1978; Schlussel et al. 1990).

Within the framework of renewal surface models, the molecular sublayer thickness δ_ν at the water side of the sea surface can be introduced as (see, e.g., Kudryavtsev and Soloviev (1985, and their references to the prior works)

$$\delta_\nu \propto (\nu_w t_*)^{1/2}, \tag{5.1}$$

where t_* is a characteristic time between successive disruptions of the molecular sublayer and ν_w is the water molecular viscosity. In the turbulent flow over a smooth surface, the mechanism of such disruptions is shear instability of the molecular sublayer, and the mean period between successive disruptions is $t_* \approx 10^2\nu_w/v_*^2$, which with (5.1) leads to $\delta_\nu \propto \nu_w/v_*$. At low wind speeds, cooling of the water surface due to evaporation causes convective thermal instability of the molecular sublayer, which creates another time scale: the scale of its disruption (for more details and references, see, e.g., Kudryavtsev and Soloviev 1985; Soloviev and Schluessel 1994). As discussed above (see also Fig. 5), at moderate and strong winds, wind waves support a significant part of the surface stress. Therefore, we may expect that at moderate and strong winds the shear stress inside the molecular sublayer is relatively weak, and other mechanisms other than shear instability should be responsible for its disruption. As mentioned above, microscale breaking disrupts the molecular sublayer and provides additional turbulent mixing beneath the surface, which is more efficient than shear production (see Fig. 6). Siddiqui et al. (2002) found that microscale breaking produces strong vortices that disrupt the molecular sublayer and generate enhanced turbulence immediately below the surface. They concluded that at low and moderate wind speeds this subsurface turbulence determines the heat and gas transfer rate, and they found that heat transfer velocity K_H is proportional to the RMS turbulent velocity just beneath the surface.

We adopt this experimental finding by Siddiqui et al. (2002) as the starting point in our further study, assuming that heat transfer velocity $K_H \propto q_0$, where q_0 is a turbulent velocity scale specified by Eq.(4.1) at the surface (at $z \to 0$). Because transfer velocity K_H is linked to the time scale of molecular sublayer disruption t_* as $t_* \propto \nu_w/K_H^2 \propto \nu_w/q_0^2$, and using (5.1), we arrive at

$$\delta_\nu = c_\nu \nu_w/q_0, \tag{5.2}$$

where c_ν is a constant. If the effect of wave breaking disappears, then $q_0 = v_*$, and Eq. (5.2) must turn into the classical relation for the viscous sublayer thickness in the wall boundary layer over a smooth surface, where $c_\nu \approx 10$. This value of c_ν is assigned in the present study.

There are two options of how to take into account the molecular sublayer in our problem: the first is to introduce a two-layer model where momentum and TKE conservation Eqs. (3.15) and (4.1) are valid at $z > \delta_\nu$, and at $z < \delta_\nu$ the turbulence mixing disappears and shear stress is supported by molecular viscosity; the second is to introduce a smooth transition between turbulent and molecular transfers by modifying the turbulent mixing length, as had been suggested by Van Driest (1956), for example. For the sake of clarity, we have chosen the first option. The velocity profile inside the viscous sublayer reads

$$w(z) = w_\delta + \frac{\tau - \tau^{\mathrm{wb}}}{\nu_w}(\delta_\nu - z), \tag{5.3}$$

where w is the complex current velocity and w_δ is the current velocity at $z = \delta_\nu$. By definition, (5.3) provides continuity of the turbulent momentum flux at $z = \delta_\nu$ specified by (5.2).

b. Comparison with the near-surface drift data

Wind drift of the surface slick shown in Fig. 4 may be used to assess the validity of our assumptions on vertical profiles of the current immediately beneath the surface. If we assume that the analogy with a turbulent boundary layer over a smooth surface is valid, then the velocity drop $u_s - u_\delta$ over the molecular sublayer itself should be $(u_s - u_\delta) \approx c_\nu v_*$ [see (5.3)], that is, about 1.3% of wind speed. This estimate is 2 times larger than the observed velocity drop over the uppermost 0.5 m shown in Fig. 4. Thus we may presume that under real conditions, wave breaking (including small-scale breaking) significantly affects the velocity profile beneath the surface. Dashed and solid lines in Fig. 4 show model simulations of the slick velocity drift with respect to the 0.5 m for two inverse wave ages $U_{23}/c_p = 1$ and 3, which corresponds to the range of U_{23}/c_p in the slick experiments. Overall, the model is consistent with the data, predicting rather weak wind drift of the sea surface relative to 0.5-m depth (drift coefficient is about 0.7%).

Cheung and Street (1988) carefully measured the velocity defect at the water surface in the laboratory experiment, which gives an extra opportunity to check the model. Figure 10 shows the wind current velocity defect with respect to the surface velocity $\Delta u(z) = u_s - u(z)$ measured by Cheung and Street (1988) in laboratory conditions (see their Fig. 1). As reported, the Stokes drift was subtracted from these data. Only the data when wind waves were observed visually are shown in this figure. Conditions of Cheung and Street (1988) experiments are summarized in Table 1. In Fig. 10, the data are presented in the coordinate system for a wall turbulent boundary layer over the smooth surface. The universal velocity profile in the boundary layer of this kind is shown by a thin dashed line. As noted by Cheung and Street (1988), the measurements in this coordinate system do not collapse, and, except data at $U = 2.6\ \mathrm{m\,s^{-1}}$, they lie well below the universal law. The observed departure of velocity profiles from the smooth surface prediction is usually associated with an increase of the surface roughness.

Predictions of the model for this experiment were calculated for water friction velocity v_* and frequencies of the wind-wave's spectral peak f_p listed in Table 1. At the lowest wind speed $U = 2.6\ \mathrm{m\,s^{-1}}$, the wavenumber

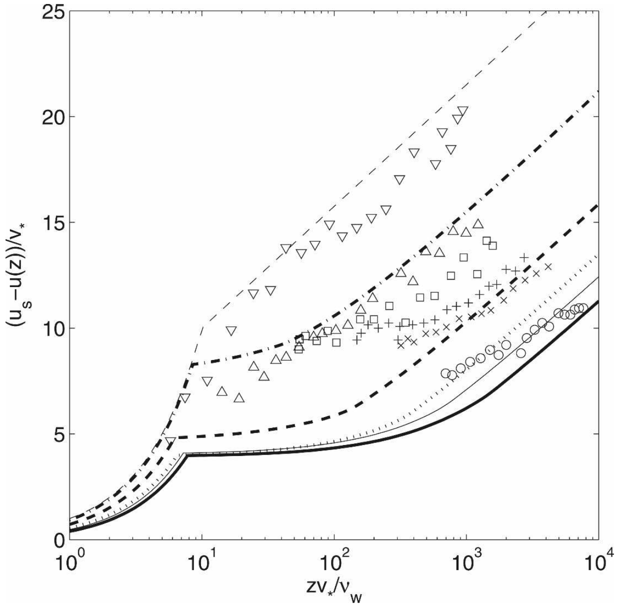

FIG. 10. Current velocity defect in laboratory conditions at various wind speed. Symbols represent measurements by Cheung and Street (1988): 2.6 (nabla), 3.2 (triangle), 4.7[1] (square), 6.7 (plus), 9.9 (cross), and 13.1 m s^{-1} (circle). Conditions of the experiment are listed in Table 1. Curves show model predictions for different wind speeds (water friction velocities) listed in Table 1: 3.2 (dashed–dotted), 4.7 (dashed), 6.7 (dotted lines), 9.9 (thin solid), and 13.1 m s^{-1} (thick solid). Thin dashed line indicates velocity profile over a smooth surface: $[u_s - u(z)]/v_* = z^+$ at $z^+ < 10$, and $[u_s - u(z)]/v_* = 10 + 1/\kappa \ln(z^+/10)$ at $z^+ > 10$.

of the spectral peak is $k_p \approx 150$ rad m^{-1}, and this value exceeds $k_{\rm wb} = k_\gamma/3 \approx 120$ rad m^{-1}, which is in our model the short wavenumber cutoff for breaking waves. Therefore, there is no effect of wave breaking at this wind speed, and the model, expectedly, predicts a profile corresponding to the universal law plotted in Fig. 10. Other curves show model predictions for higher wind speeds, where microbreaking and breaking are essential. The model qualitatively reproduces the behavior of velocity defect profiles with a wind speed increase. According to the model, the observed deviation of the velocity profiles from the universal law for the smooth surface is caused by direct injection of momentum and energy from small-scale breaking into the water body. Though the water surface remains smooth (because we introduced the molecular sublayer), enhanced turbulence mixing straightens velocity profiles and makes the molecular sublayer thinner. These factors result in a trend of velocity profiles that is usually associated with increasing "aerodynamic" roughness of the sea surface. Notice that well below the water surface, the model velocity profiles can apparently be fitted by log law. The intersection of the log law with the z axis gives a water surface roughness scale. However, an advantage of our model is that it describes the fine structure of a subgrid surface roughness, which may be of crucial importance for many transfer processes at the air–sea interface.

TABLE 1. Conditions of the Cheung and Street (1988) experiment.

U (m s^{-1})	u_s (m s^{-1})	v_* (m s^{-1})	f_p (Hz)
2.6	0.07	0.0034	6.1
3.2	0.070	0.0049	5.2
4.7	0.093	0.0070	3.5
6.7	0.137	0.0112	2.7
9.9	0.204	0.0175	2.4
13.1	0.270	0.0275	2.0

6. Concluding remarks

The starting point of our study was a dedicated field experiment. Analysis of drifter measurements in the uppermost 5-m layer showed that the wind-driven current velocity gradients are 2 to 5 times weaker than in the corresponding wall boundary layer. We attribute weak velocity gradients to enhanced turbulent mixing due to wave breaking, despite the fact that the breaking events (as white caps) were relatively rare or even visually absent at low winds. In this sense, our results are consistent with experimental evidence on the enhanced rate of TKE dissipation in the upper ocean (e.g., Agrawal et al. 1992; Terray et al. 1996; Drennan et al. 1996). Besides, our measurements showed that the velocity defect between the sea surface (identified by tracing drift of an artificial slick) and 0.5-m depth normalized by wind speed is about 0.7%. This estimate is even smaller than the anticipated velocity drop over the molecular sublayer, which should be on the order of $10v_*$ or about 1% of wind speed.

To interpret available observations, we proposed a semiempirical model based on taking into account the effect of wave breaking on wind-driven current and turbulence. The model develops the idea suggested by Kitaigorodskii (1984) and Terray et al. (1996) of direct injection of momentum and energy by breaking waves into the water body by proposing a mathematical formulation of the idea and by extending it for situations with no visible breakings. One of the key novel features is that we apply this approach for wave breaking of all scales, including small-scale breaking. This is prompted by experimental finding by Zhang and Cox (1999), Siddiqui et al. (2002), Zappa et al. (2002), and Siddiqui and Loewen (2007), who showed that small-scale breaking (generating parasitic capillaries) produces intensive vortices that provide strong mixing beneath the surface. We assumed that a breaking wave injects its momentum and energy into a layer of depth about its inverse wavenumber. We took this effect into account by introducing wave-breaking momentum and energy fluxes into the momentum and TKE conservation equations, supplemented by the Kolmogorov–Prandtl closure scheme. To parameterize intensive subsurface vortices produced by microscale breaking, we have modified the mixing length, assuming that beneath the surface it corresponds to the inverse wavenumber of the smallest breaking waves. At large depths, the mixing length is bounded by a value proportional to v_*/f—the Ekman boundary layer scale (Zilitinkevich and Esau 2005).

As expected, the rate of production of turbulence by wave breaking is much stronger than the shear production, which results in enhanced turbulent mixing in the wave-stirred layer and a dramatic deviation of its vertical structure from the wall boundary layer law. The proposed model is able to consistently describe our observations, in particular, a weak current velocity gradient in the upper layer, as well as available experimental field data on the enhanced rate of TKE dissipation.

In our model development we did not need an introduction of a roughness length, which would be neither similar to the Charnock roughness scale nor proportional to the significant wave height. The latter is widely used in the upper ocean current and turbulence modeling (e.g., Drennan et al. 1996; Craig and Banner 1994; Stacey, 1999; Soloviev and Lukas, 2003; Rascle et al. 2006). However, the shortcomings of such an approach are that the uppermost layer of the ocean remains simply unresolved and all physical processes occurring beneath the surface are treated as subgrid processes. Instead, we took into account that from the "top" the sea surface is covered by the molecular sublayer, which is a routinely observed phenomenon referred to as a cool skin. Its thickness depends on the turbulence intensity beneath, and the velocity drop over this layer is governed by tangential stress acting on the surface from the air side.

We would like to emphasize that the pretty bold assumptions we made about turbulence generated by the capillaries and the choice of the cutoff scale have been justified by our comparison with the very careful laboratory experiment by Cheung and Street (1988). Note that Siddiqui and Loewen (2007) reported another set of extensive laboratory investigations on the effect of small-scale breaking on TKE and wind-driven current. However, because Siddiqui and Loewen's (2007) study appeared when the present paper had been already submitted, any detailed discussion of their findings was not possible.

The proposed model certainly has room for further development. In particular, in our study for the sake of simplicity we neglected diffusion of turbulence. It could and should be taken into account with the price being the necessity to solve the momentum and TKE conservation equations numerically. We adopted Phillips's (1985) hypothesis on the spectral distribution of breakings fronts for the full range of wind waves. Once there is a better estimate for the breaking distribution, it is straightforward to incorporate it into the model. Similarly, a more elaborate parameterization of mixing caused by breaking events could be developed, dependent on the progress in direct numerical simulation of breaking along the lines of Sullivan et al. (2004). However, even in its present form the model can already be consistently used for investigation of both the upper ocean dynamics and small-scale processes of momentum, heat, and gas transfer. In particular, because the model links the transfer with the current vertical profile potentially measurable today by modern HF radars (e.g., Teague 1986; Shrira et al. 2001), this paves the way for employing an established remote sensing technique to monitor earlier inaccessible characteristics of air–sea interaction.

Acknowledgments. The work would not have been possible without support from INTAS under Grants 97-575 and 01-234, 05-2206 8014. In the final stage, this study was supported by ESA through OSCSAR Project under the ESA-IAF programe on GMES Networking with Russia and Ukraine. VK also acknowledges the support from IFREMER under Project 2006-20712141. The authors are very grateful to Alexander Bol'shakov and Vladimir Smolov for their technical assistance in carrying the drifter experiments, without their skill, dedication, and perseverance the experiment would never have succeeded.

APPENDIX A

The Experiment

The experiments were carried out in the summer periods of 2000, 2001, and 2004 around the MHI Black Sea platform (44°24′N, 33°59′E). A map of the experimental area and a scheme of the experiment are shown in Fig. A1. The vertical profile of surface current velocity was measured using six drifters deployed from a boat 1–2 km offshore. The depth of the sea always exceeded 50 m, which presumably does not affect the dynamics of the uppermost few meters we are interested in.

Measurements of the current velocity below the wavy surface by means of Lagrangian drifters is a well-established technique (see, e.g., Churchill and Csanady 1983; Csanady 1984; Kudryavtsev and Soloviev 1990;

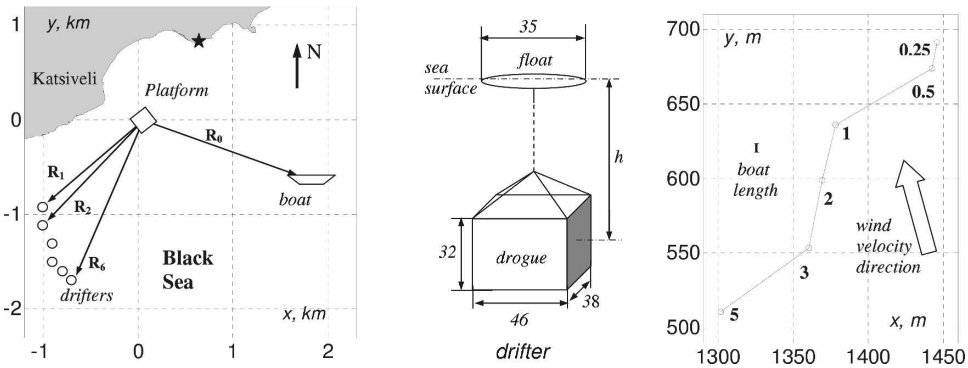

FIG. A1. (left) Map of the experimental area, (middle) design of a drifter used in the experiments and its geometrical parameters in cm, and (right) an example of the drifters position before their picking up (right plot).

Kudryavtsev et al. 1996. and references therein) and is the most appropriate in our context. Because the highest vertical shear occurs in the immediate vicinity of the surface, any fixed Eulerian devices are not suitable for measurements of vertical shear profiles in the uppermost meter. The existing acoustic Doppler current profilers (ADCPs) usually do not resolve the uppermost 0.5–1 m, which are crucial for our study (e.g., Ivonin et al. 2004). The techniques of estimating vertical profiles of surface currents in the uppermost meter based on HF radars, in fact, estimate several integrals of vertical profile of current with certain weighting functions, and to recover the current profile one needs some a priori knowledge of the shape of the profile (Shrira et al. 2001; Teague 1986).

The design of the drifter employed in our experiments and its geometrical parameters are given in Fig. A1 (middle). The drifter consists of a surface float and drogue connected by a thin steel cable. The drogue has a form of a box with the top and bottom knocked out. Six drifters with different depths of the drogues were used. The depth of the drogue h_i is defined as a distance from its geometric center to the surface and was equal to $h_i = 0.25, 0.5, 1.0, 2.0, 3.0$, and 5.0 m. The effective section of the drogue is about 50 times larger than that of the surface float. Thus, the drifter follows the current velocity at the depth of the drogue. The procedure of currents measurements is sketched in Fig. A1. The drifters were simultaneously deployed from the boat at a distance of about 2 km away from the platform. Coordinates of this point $\mathbf{R}_0 = (x_0, y_0)$ were determined by a laser range finder installed on the platform. After about 30 to 60 min, the time interval was chosen to be large enough to have a distance between the drifters on the order of 100 m, the boat traveled over all the drifters and successively picked them up at corresponding time Δt_i. Coordinates $\mathbf{R}_i = (x_i, y_i)$ of the picking up of each of the drifters were determined by the same laser range finder from the platform. Velocity of an ith drifter was estimated as

$$\mathbf{u}_i = \frac{\mathbf{R}_i - \mathbf{R}_0}{\Delta t_i}. \tag{A.1}$$

An example of the drifter scatter before their picking up is shown in Fig. A1. For comparison, the boat length is also shown in this figure. Velocity of each drifter is interpreted as the current velocity at the drogue depth. The error $|\delta\mathbf{u}_i|$ in estimating of $\mathbf{u}_i$ results primarily from the "finite" length l of the boat ($l = 7$m), $|\delta\mathbf{u}_i|$ can be estimated as $|\delta\mathbf{u}_i| \approx \pm(l/2)/\Delta t_i$, which at $\Delta t_i = 30$ min gives $||\delta\mathbf{u}_i| \approx \pm 2 \times 10^{-3}$ m s^{-1}.

Note that due to its size the drogue filters wave-induced velocity oscillations with wavenumbers exceeding $k > 1/l_{\max}$, where $l_{\max}$ is the maximal scale of the drogue. At $l_{\max} = 0.46$ m the cutoff wavelength $\lambda_{\text{cut-off}}$ is about $\lambda_{\text{cut-off}} \approx 3$ m. Our estimates showed that the relaxation time of the drogue (its inertia) is much less than the period of the cutoff surface wave. Therefore, we assume that the drogue follows both mean currents and wave-induced motions caused by surface waves with $k < 1/l_{\max}$. The latter presumes that the drogue may possess a mean Lagrangian wave velocity u_{dr} similar to the Stokes drift of dominant surface waves. This mean Lagrangian horizontal velocity of a drifter is defined as $u_{\text{dr}} = \overline{u(\mathbf{r}, t)}$, where u is the Eulerian velocity, $\mathbf{r}$ is the radius vector of drogue, which can be represented as the sum of mean $\bar{\mathbf{r}}$ and wave-induced oscillations $\tilde{\mathbf{r}}$, $\mathbf{r} = \bar{\mathbf{r}} + \tilde{\mathbf{r}}$. In the second order of wave steepness, the drifter velocity reads

$$u_{\text{dr}} = \overline{u(\mathbf{r}, t)} \approx \bar{u}(z) + \overline{\frac{\partial \tilde{u}}{\partial x}\tilde{r}_x} + \overline{\frac{\partial \tilde{u}}{\partial z}\tilde{r}_z}, \tag{A.2}$$

where $\bar{u}$ is the mean velocity, $\tilde{u}$ is the wave horizontal velocity, and $\tilde{r}_x$, $\tilde{r}_z$ are wave-induced horizontal and ver-

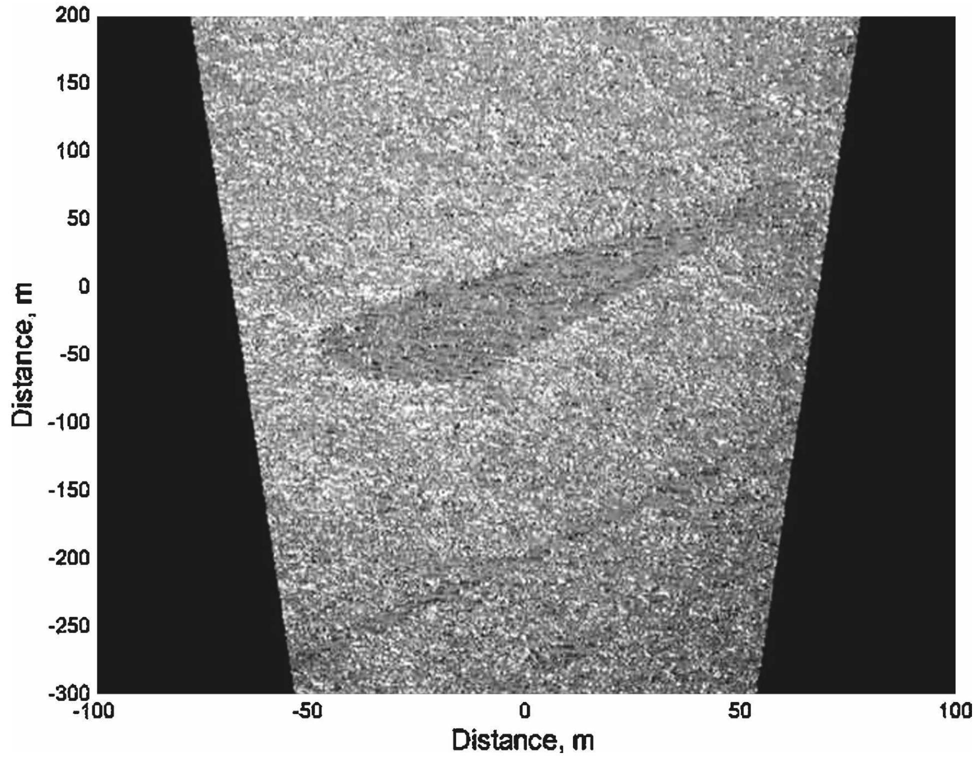

FIG. A2. Fragment of a photograph (transformed to the orthophotograph) of the sea surface containing the artificial slick. Photographing made by digital camera from the rock (altitude 153 m) indicated in (left) Fig. A1 by a star.

tical displacements of the drogue. Because the drogue is linked to the surface float, $\tilde{r}_z$ is equal to the wave surface displacement, while $\tilde{r}_x$ corresponds to the local horizontal wave displacement. If a, k, and c are amplitude, wavenumber, and phase velocity of a monochromatic wave, then the drifter's Lagrangian velocity (A.2) is

$$u_{\mathrm{dr}}(z) = \overline{u}(z) + u_{\mathrm{St}}(z),$$

$$u_{\mathrm{St}}(z) = a^2k^2c(e^{-kz} + e^{-2kz})/2. \qquad \text{(A.3)}$$

Thus the drifter velocity consists of the mean Eulerian velocity $\overline{u}(z)$ and a quasi-Stokes velocity component $u_{\mathrm{St}}(z)$. The latter differs from the classical Stokes drift velocity by the shape of vertical attenuation [a sum of two exponents instead of a single one: $\exp(-2kz)$].

The experiments of 2004 and 2005 were supplemented by the measurements of the velocity at the sea surface. The artificial surface slick was chosen as a "tracer" of the surface currents. The artificial slick was produced by a vegetable oil spilled from the boat (the spilled volume was 170 cm^3). With time, the oil spread on the surface and, due to suppression of short wind waves, formed a well-visible surface slick. Drift of the slick was observed by means of photography of the sea surface by the digital camera Olympus C750Z from a shore cliff of altitude 153 m. The cliff is indicated by a small asterisk at the top left in Fig. 1A. Evolution of the geometric properties of the slick (such as its area and configuration parameters) is reported in Malinovsky et al. (2007). In the present study, we shall use only its mean drift velocity defined through the coordinates of its "center of mass." To determine the center and its coordinates (with respect to the platform), each of the images was transformed to the orthophotograph. A fragment of the transformed image containing the slick is shown in Fig. A2. Coordinates of the slick at the beginning and the end of the survey (this time interval was the same as for the drifters) were used to assess the surface drift velocity via (A.1). Only two drifters at depths 0.5 and 5 m were used in the experiments with the slicks.

The measurements of surface currents were accompanied by measurements of the water temperature profiles in the upper 10 m taken from the boat (with discreteness over depths of 0.5 m), measurements of wind velocity and air temperature from the platform at height 23 m, and surface waves were measured by an array of six resistance wave gauges (except 2000 when sea state was observed visually). The wave gauges enabled us to estimate 2D wave spectra, and thus to discriminate wind seas and swell. In the present study, we analyze the data obtained at conditions of on-shore winds only and at almost neutral stratification of the sea upper layer—when the temperature drop within the upper 10 m did not exceed 0.1°C. By selecting these data we are trying to filter out the effects of the diurnal heating, which may significantly affect dynamics of the upper layer at low wind (e.g., Kudryavtsev and Soloviev 1990; Kudryavtsev et al. 1996).

APPENDIX B

Estimate of Momentum and Energy Flux Spent on Wave Development

Let us estimate the share of the energy and momentum fluxes spent on the wave field development (F^d and τ^d, respectively) with respect to the energy F^w and momentum τ^f fluxes coming from the wind. These quantities are estimated as

$$(F^d, \tau^d) = \int c_g \partial(E, M)/\partial x_1 \, d\mathbf{k}, \qquad \text{(B.1)}$$

$$(F^w, \tau^f) = \int \beta\omega(E, M) \, d\mathbf{k}, \qquad \text{(B.2)}$$

where $E(\mathbf{k})$ and $M(\mathbf{k}) = k_1/\omega E(\mathbf{k})$ are the wave energy and momentum spectra, respectively, $\beta = c_\beta(u_*/c)^2 \cos^2\varphi$ is the wind wave growth rate (at $-\pi/2 \le \varphi \le \pi/2$), c_β is the growth rate constant, and φ is the angle between vector $\mathbf{k}$ and wind direction (Plant 1982; see also Kudryavtsev and Makin 2004 for justification of the angular distribution of β). Ratios of the advective energy and momentum fluxes (B.1) to the corresponding wind fluxes (B.2) calculated for the original JONSWAP spectrum (see, e.g., Komen et al. 1994) as a function of inverse wave age U_{10}/c_p for wind speeds 5, 10, and 20 m s^{-1} are shown in Fig. 5. To have a smooth transition from young to mature seas, in these calculations dependence of U_{10}/c_p on fetch is specified as (Elfouhaily et al. 1997):

$$U_{10}/c_p = 0.84\,[\tanh(\hat{x}/\hat{x}_0)^{0.4}]^{-0.75},$$

where $\hat{x} = xg/U_{10}^2$ is the dimensionless fetch $\hat{x}_0 = 2.2 \times 10^4$.

REFERENCES

Agrawal, Y. C., E. A. Terray, M. A. Donelan, P. A. Hwang, A. J. Williams, W. M. Drennan, K. K. Kahma, and S. A. Kitaigorodskii, 1992: Enhanced dissipation of kinetic energy beneath surface waves. *Nature,* **359,** 219–220.

Anis, A., and J. N. Moum, 1995: Surface wave–turbulence interactions: Scaling ε(z) near the sea surface. *J. Phys. Oceanogr.,* **25,** 2025–2045.

Benilov, A. Y., and L. N. Ly, 2002: Modeling of surface waves breaking effects in the ocean upper layer. *Math. Comput. Model.,* **35,** 191–213.

Cheung, T. K., and R. L. Street, 1988: The turbulent layer in water at an air-water interface. *J. Fluid Mech.,* **194,** 133–151.

Churchill, J. H., and G. T. Csanady, 1983: Near-surface measurements of quasi-Lagrangian velocities in open water. *J. Phys. Oceanogr.,* **13,** 1669–1680.

Craig, P. D., 1996: Velocity profiles and surface roughness under breaking waves. *J. Geophys. Res.,* **101,** 1265–1277.

——, and M. L. Banner, 1994: Modeling wave-enhanced turbulence in the ocean surface layer. *J. Phys. Oceanogr.,* **24,** 2546–2559.

Csanady, G. T., 1984: The free surface turbulent shear layer. *J. Phys. Oceanogr.,* **14,** 402–411.

Drennan, W. M., K. K. Kahma, E. A. Terray, M. A. Donelan, and S. A. Kitaigorodskii, 1992: Observations of the enhancement of kinetic energy dissipation beneath breaking wind waves. *Breaking Waves,* M. L. Banner and R. H. J. Grimshaw, Eds., Springer-Verlag, 95–101.

——, M. A. Donelan, E. A. Terray, and K. B. Katsaros, 1996: Oceanic turbulence dissipation measurements in SWADE. *J. Phys. Oceanogr.,* **26,** 808–815.

Elfouhaily, T., B. Chapron, K. Katsaros, and D. Vandermark, 1997: A unified directional spectrum for long and short wind driven waves. *J. Geophys. Res.,* **102,** 15 781–15 796.

Gemmrich, J. R., and D. M. Farmer, 2004: Near-surface turbulence in the presence of breaking waves. *J. Phys. Oceanogr.,* **34,** 1067–1086.

Gill, A. E., 1982: *Atmosphere–Ocean Dynamics*. Academic Press, 662 pp.

Ivonin, D. V., P. Broche, J.-L. Devenon, and V. I. Shrira, 2004: Validation of HF radar probing of the vertical shear of surface currents by acoustic Doppler current profiler measurements. *J. Geophys. Res.,* **109,** C04003, doi:10.1029/2003JC002025.

Kitaigorodskii, S. A., 1984: On the fluid dynamical theory of turbulent gas transfer across an air–sea interface in the presence of breaking wind waves. *J. Phys. Oceanogr.,* **14,** 960–972.

——, 1994: A note on the influence of breaking wind waves on the aerodynamic roughness of the sea surface as seen from below. *Tellus,* **46A,** 681–685.

——, M. A. Donelan, J. L. Lumley, and E. A. Terray, 1983: Wave–turbulence interactions in the upper ocean. Part II: Statistical characteristics of wave and turbulent components of the random velocity field in the marine surface layer. *J. Phys. Oceanogr.,* **13,** 1988–1999.

Komen, G. J., L. Cavaleri, M. Donelan, K. Hasselmann, S. Hasselmann, and P. A. E. M. Janssen, 1994: *Dynamics and Modelling of Ocean Waves*. Cambridge University Press, 540 pp.

Korotaev, G. K., Yu. M. Kuftarkov, and A. I. Fel'senbaum, 1976: On dynamical structure of the near-surface layer of the ocean (in Russian). *Dokl. Akad. Nauk SSSR,* **231,** 121–125.

Kudryavtsev, V. N., and A. Soloviev, 1985: On thermal state of the ocean surface. *Izv. Acad. Sci. USSR Atmos. Oceanic Phys.,* **17,** 1065–1071.

——, and ——, 1990: Slippery near-surface layer of the ocean arising due to daytime solar heating. *J. Phys. Oceanogr.,* **20,** 617–628.

——, and V. Makin, 2001: The impact of air-flow separation on the drag of the sea surface. *Bound.-Layer Meteor.,* **98,** 155–171.

——, and ——, 2004: Impact of swell on marine atmospheric boundary layer. *J. Phys. Oceanogr.,* **34,** 934–946.

——, A. Tsvetkov, and S. Grodsky, 1996: Diurnal heating of the ocean surface layer. *The Air–Sea Interface: Radio and Acoustic Sensing, Turbulence and Wave Dynamics,* M. A. Donelan, W. H. Hui, and W. J. Plant, Eds., The University of Toronto Press, 549–556.

——, D. Akimov, J. A. Johannessen, and B. Chapron, 2005: On radar imaging of current features. 1. Model and comparison with observations. *J. Geophys. Res.,* **110,** C07016, doi:10.1029/2004JC002505.

Longuet-Higgins, M. S., 1992: Capillary rollers and bores. *J. Fluid Mech.,* **240,** 659–679.

——, 1996: The crest instability of steep gravity waves, or how do short waves break? *The Air–Sea Interface: Radio and Acoustic Sensing, Turbulence and Wave Dynamics,* M. A. Donelan, W. H. Hui, and W. J. Plant, Eds., The University of Toronto Press, 217–246.

Malinovsky V. V., V. A. Dulov, A. E. Korinenko, A. N. Bol'shakov, and V. E. Smolov, 2007: Field investigations of the drift of artificial thin films on the sea surface. *Izv. Acad. Sci. USSR, Atmos. Oceanic Phys.,* **42,** 3–12.

Mellor, G. L., and T. Yamada, 1982: Development of a turbulence closure model for geophysical fluid problems. *Rev. Geophys.,* **20,** 851–875.

Melville, W. K., 1996: The role of surface-wave breaking in air-sea interaction. *Annu. Rev. Fluid Mech.,* **28,** 279–321.

——, and P. Matusov, 2002: Distribution of breaking waves at the ocean surface. *Nature,* **417,** 58–63.

——, F. Verone, and C. J. White, 2002: The velocity field under breaking waves: Coherent structures and turbulence. *J. Fluid Mech.,* **454,** 203–233.

Phillips, O. M., 1977: *The Dynamics of the Upper Ocean*. Cambridge University Press, 336 pp.

——, 1985: Spectral and statistical properties of the equilibrium range in wind-generated gravity waves. *J. Fluid Mech.,* **156,** 505–531.

Plant, W. J., 1982: A relationship between wind stress and wave slope. *J. Geophys. Res.,* **87,** 1961–1971.

Rapp, R. J., and W. K. Melville, 1990: Laboratory measurements of deep-water breaking waves. *Philos. Trans. Roy. Soc. London,* **A331,** 735–800.

Rascle, N., F. Ardhuin, and E. A. Terray, 2006: Drift and mixing under the ocean surface: A coherent one-dimensional description with application to unstratified conditions. *J. Geophys. Res.,* **111,** C03016, doi:10.1029/2005JC003004.

Riley, D. S., M. A. Donelan, and W. H. Hui, 1982: An extended Miles theory for wave generation by wind. *Bound.-Layer Meteor.,* **22,** 209–225.

Santala, M. J., 1991: Surface-referenced current meter measurements. Ph.D. dissertation, WHOI–MIT Joint Program in Oceanography, 250 pp.

Schlussel, R., W. J. Emery, H. Grassel, and T. Mammen, 1990: On the bulk skin temperature difference and its impact on satellite remote sensing of sea surface temperature. *J. Geophys. Res.,* **95,** 13 341–13 356.

Shrira, V., D. Ivonin, P. Broche, and J. C. deMaistre, 2001: On remote sensing of vertical profile of ocean surface currents by means of single-frequency VHF radar. *Geophys. Res. Lett.,* **28,** 3955–3958.

Siddiqui, M. H. K., and M. R. Loewen, 2007: Characteristics of the wind drift layer and microscale breaking waves. *J. Fluid Mech.,* **573,** 417–456.

——, ——, C. Richardson, W. Asher, and A. Jessup, 2002: Turbulence generated by microscale breaking waves and its influence on air–water gas transfer. *Gas Transfer at Water Surface, Geophys. Monogr*., Vol. 127, Amer. Geophys. Union, 11–16.

Smith, S. D., 1998: Coefficients for the sea surface wind stress, heat flux, and wind profiles as a function of wind speed and temperature. *J. Geophys. Res.,* **93,** 15 467–15 472.

Soloviev, A., and P. Schluessel, 1994: Parameterization of the cool skin of the ocean and of the air–ocean gas transfer on the basis of modeling surface renewal. *J. Phys. Oceanogr.,* **24,** 1339–1346.

——, and R. Lukas, 2003: Observation of wave-enhanced turbulence in the near-surface layer of the ocean during TOGA COARE. *Deep-Sea Res. I,* **50,** 371–395.

Sounders, P. M., 1978: The skin temperature of the ocean: A review. *Mem. Soc. Roy. Sci. Liege,* **6,** 93–98.

Stacey, M. W., 1999: Simulation of the wind-forced near-surface circulation in Knight Inlet: A parameterization of the roughness length. *J. Phys. Oceanogr.,* **29,** 1363–1367.

Sullivan, P., J. C. McWilliams, and W. K. Melville, 2004: The ocean boundary layer driven by wave breaking with stochastic variability. Part 1: Direct numerical simulations. *J. Fluid Mech.,* **507,** 143–174.

Teague, C. C., 1986: Multifrequency HF radar observations of currents and current shears. *IEEE J. Oceanic Eng.,* **11,** 258–269.

Teixeira, M. A. C., and S. E. Belcher, 2002: On the distortion of turbulence by a progressive surface wave. *J. Fluid Mech.,* **458,** 229–267.

Terray, E. A., M. A. Donelan, Y. C. Agrawal, W. M. Drennan, K. K. Kahma, A. J. Williams, P. A. Hwang, and S. A. Kitaigorodskii, 1996: Estimates of kinetic energy dissipation under breaking waves. *J. Phys. Oceanogr.,* **26,** 792–807.

——, W. M. Drennan, and M. A. Donelan, 1999: The vertical structure of shear and dissipation in the ocean surface layer. *Proc. Symp. on the Wind-Driven Air–Sea Interface: Electromagnetic and Acoustic Sensing, Wave Dynamics and Turbulent Fluxes,* Sydney, Australia, ADFA Document Production Centre, 239–245.

Thorpe, S. A., 1984: On the determination of Kv in the near-surface ocean from acoustic measurements of bubbles. *J. Phys. Oceanogr.,* **14,** 855–863.

——, 2004: Recent developments in the study of ocean turbulence. *Annu. Rev. Earth Planet. Sci.,* **32,** 91–109.

Van Driest, E. R., 1956: On turbulent flow near a wall. *J. Aerosol Sci.,* **23,** 1007–1010.

Zappa, C. J., W. E. Asher, A. T. Jessup, J. Klinke, and S. R. Long, 2002: Effect of microscale breaking on air–water gas transfer. *Gas Transfer at Water Surface, Geophys. Monogr*., Vol. 127, Amer. Geophys. Union, 23–30.

Zhang, X., and C. S. Cox, 1999: Vortical motions under short wind waves. *Proc. Symp. on the Wind-Driven Air–Sea Interface: Electromagnetic and Acoustic Sensing, Wave Dynamics and Turbulent Fluxes,* Sydney, Australia, ADFA Document Production Centre, 277–284.

Zikanov, O., D. Slinn, and M. R. Dhanak, 2003: Large-eddy simulations of the wind-induced turbulent Ekman layer. *J. Fluid Mech.,* **495,** 343–368.

Zilitinkevich, S., and I. Esau, 2005: Resistance and heat transfer laws for stable and neutral planetary boundary layers: Old theory advanced and re-evaluated. *Quart. J. Roy. Meteor. Soc.,* **131,** 1863–1892.